

## Numerical modelling of cancellous bone damage using an orthotropic failure criterion and tissue elastic properties as a function of the mineral content and microporosity

Raquel Megías<sup>a</sup>, Ana Vercher-Martínez<sup>a,\*</sup>, Ricardo Belda<sup>a</sup>, José Luis Peris<sup>b</sup>, Ricardo Larrainzar-Garijo<sup>c</sup>, Eugenio Giner<sup>a</sup>, F. Javier Fuenmayor<sup>a</sup>

<sup>a</sup> Dept. de Ingeniería Mecánica y de Materiales. Instituto de Ingeniería Mecánica y Biomecánica de Valencia - I2MB, Universitat Politècnica de València, Camino de Vera, Building 5E-9C, Valencia 46022, Spain

<sup>b</sup> Instituto de Ingeniería Mecánica y Biomecánica de Valencia - I2MB, Healthcare Technology Group (GTS-IBV), Universitat Politècnica de València, Camino de Vera, Building 5E-9C, Valencia 46022, Spain

<sup>c</sup> Orthopedic and Trauma Department, Hospital Universitario Infanta Leonor, Medical School, Universidad Complutense Madrid, Spain



### ARTICLE INFO

#### Article history:

Received 22 September 2021

Revised 7 March 2022

Accepted 18 March 2022

#### Keywords:

Lamellar bone porosity  
Cancellous bone numerical modelling  
Finite element method  
Damage initiation  
Material property degradation  
Orthotropic failure criterion

### ABSTRACT

**Background and objective:** Elastic and strength properties of lamellar tissue are essential to analyze the mechanical behaviour of bone at the meso- or macro-scale. Although many efforts have been made to model the architecture of cancellous bone, in general, isotropic elastic constants are assumed for tissue modelling, neglecting its non-isotropic behaviour. Therefore, isotropic damage laws are often used to estimate the bone failure. The main goals of this work are: (1) to present a new model for the estimation of the elastic properties of lamellar tissue which includes the bone mineral density (BMD) and the microporosity, (2) to address the numerical modelling of cancellous bone damage using an orthotropic failure criterion and a discrete damage mechanics analysis, including the novel approach for the tissue elastic properties aforementioned.

**Methods:** Numerical homogenization has been used to estimate the elastic properties of lamellar bone considering BMD and microporosity. Microcomputed Tomography ( $\mu$ -CT) scans have been performed to obtain the micro-finite element ( $\mu$ -FE) model of cancellous bone from a vertebra of swine. In this model, lamellar tissue is orientated by considering a unidirectional layer pattern being the mineralized collagen fibrils aligned with the most representative geometrical feature of the trabeculae network. We have considered the Hashin's failure criterion and the Material Property Degradation (MPDG) method for simulating the onset and evolution of bone damage.

**Results:** The terms of the stiffness matrix for lamellar tissue are derived as functions of the BMD and microporosity at tissue scale. Results obtained for the apparent yield strain values agree with experimental values found in the literature. The influence of the damage parameters on the bone mechanics behaviour is also presented.

**Conclusions:** Stiffness matrix of lamellar tissue depends on both BMD and microporosity. The new approach presented in this work enables to analyze the influence of the BMD and porosity on the mechanical response of bone. Lamellar tissue orientation has to be considered in the mechanical analysis of the cancellous bone. An orthotropic failure criterion can be used to analyze the bone failure onset instead of isotropic criteria. The elastic property degradation method is an efficient procedure to analyze the failure propagation in a 3D numerical model.

© 2022 Elsevier B.V. All rights reserved.

## 1. Introduction

Cancellous bone is a highly porous and heterogeneous material with varying material properties [1], mainly found at the epiphysis and metaphysis of long bones and in the vertebral bodies. Adult bone tissues, both cortical and cancellous, are laminated at

\* Corresponding author.

E-mail address: [anvermar@dimm.upv.es](mailto:anvermar@dimm.upv.es) (A. Vercher-Martínez).

the microscale [2]. The tissue arranged at these layers is the so-called lamellar bone tissue, being the mineralized collagen fibrils its main constituent. Consequently, strength and stiffness properties of lamellar tissue are essential to analyze the mechanical behaviour of bone at the meso and macro-scale. In the lamellar tissue, mineralized fibre bundles, embedded in the extra-fibrillar matrix, confer a predominant orthotropic symmetry [3–5] leading to an anisotropic behaviour under generic multi-axial loading.

On the other hand, the mineral content and the porosity at lamellar tissue level (microporosity) are two essential parameters related with the bone mechanics behaviour. It is well known that an increase in the volumetric bone mineral density (BMD) has a direct implication on the rise of the stiffness and, if it is excessive (i.e. due to the absence of bone resorption in the bone turnover process) the tissue will become more brittle [6–9].

Regarding the microporosity, it also contributes to decline the mechanical response of bone tissue. Several agents contribute to the microporosity increase [10]: old age, estrogen deficiency in post-menopausal women, glucocorticoids and immobilization. In addition, when a rapid bone loss is prevalent (commonly after menopause), depth cavities may occur due to an excessive osteoclastic resorption leading to the trabecular bone perforation of structural elements causing the loss of the structural continuity [11]. Osteoclastic perforation was also observed by [12] in a scanning electron microscope study of the remodelling process of vertebral trabecular bone. In [13] two types of resorption lacunae in trabecular bone were observed. Moreover, lacunar and tunnelling perforation are distinguished denoting microstructural changes, related with disturbed bone turnover. Advances in computer tomography techniques have shown that porosity is responsible of a substantial amount of bone loss and consequently, the resultant higher bone fragility and mechanical competence deterioration.

The non-isotropic nature of lamellar tissue is also a relevant aspect to be included in the quantification of bone mechanical properties. In the review of biomechanics and mechanobiology of trabecular bone presented in Oftadeh et al. [14], it is stated that at the microstructural scale, trabeculae consist of groups of parallel lamellae bounded by cement lines primarily oriented also parallel to the trabecular surfaces. In addition, the three-dimensional ultrastructure bone arrangement in relation to the local trabecular direction is analyzed in Georgiadis et al. [15]. They state that bone ultrastructure is mostly aligned to trabecular microstructure near trabecular surface. However, when going towards trabecular core, the ultrastructure alignment decreases to around 40%.

Cancellous tissue was characterized as a microstructure consisting of layers interspersed with transition zones where the proportions of collagen and mineral vary [16]. Hosaka-Takamiya et al. [17] observed that collagen bundles in trabecular bone run along the long axis of the trabecula. In [18], the fibril orientation is addressed in a numerical model of trabecular bone.

In the study presented by Rami et al. [19], a three dimensional multiscale micromechanical model, where the lamellar tissue is modelled as a multilayered laminate, is suggested. The mineralized collagen fibrils follow a determined angular orientation pattern. That work deals with the linear anisotropic mechanical properties of the cancellous bone, no strength analysis is performed.

In the literature we find several references that reveal the importance of considering the tissue properties in the trabecular bone numerical models, when the mechanical competence of bone is under study. Hammond et al. [20] state that, only when the tissue anisotropy is considered in their numerical models, the shape and distributed microcracking typically observed in trabecular bone are reproduced. In [18], the effect of tissue properties on predicted stresses and strains is observed. This improves the correlation between the solution from numerical models with experimental data. For example, material heterogeneity seems to play an

important role in resisting bone damage under cyclic loads with long service lives [21]. In addition, in Renders et al. [22], the authors demonstrate that the no consideration of the mineralization heterogeneity overestimates the apparent Young's moduli.

With the recent advances in acquisition techniques of high-resolution medical image and postprocessing software, the numerical analysis of the strength of trabecular bone through  $\mu$ -FE models has become an interesting option. Non-linear  $\mu$ -FE models were used to simulate pre- and post-yielding cancellous bone behaviour [23–28].

In this numerical context, an interesting option to simulate the bone failure is the Continuum Damage Mechanics (CDM) approach. In this approach, the initiation and propagation of cracks is based on a smeared crack approach [25,26,29–31]. In a quasi-static loading case, isotropic damage laws are often used to represent the non-linear behaviour of cancellous bone [25,27]. In addition, finite element deletion technique is also considered to model the complete fracture of the trabeculae [26].

Concerning the strength of trabecular bone, a detailed review of several failure criteria applied in material science is reported in Oftadeh et al. [14], that have been considered for the study of the bone mechanics under multi-axial stresses. In that work, it is also highlighted that bone mechanical behaviour is highly dependent on tissue properties.

In order to implement a damage evolution law in a three-dimensional numerical analysis, the Material Property Degradation (MPDG) is a procedure very efficient computationally. This method can simulate the post-damage degradation of brittle anisotropic materials. The MPDG results in a non-linear evolution where the damage variable,  $d$ , takes predefined discrete values depending on the dominant failure mode, and assumes an instant stiffness reduction of the material. In contrast, in the Continuum Damage Mechanics (CDM) approach, the damage variable gradually increases with the amount of fracture energy dissipated. The discrete damage method is also applied to the study of progressive failure in laminate structures.

The main contributions of the approach presented in this work can be summarized in: (1) it addresses the numerical modelling of the cancellous bone mechanical behaviour, not only considering the microstructure, as usually done in literature, but also the non-isotropic elastic tissue properties, as a function of BMD and microporosity. (2) It includes the orientation of the mineralized collagen fibrils in the main geometrical feature of the trabeculae network. (3) It also proposes to use an interactive failure criterion based on the inferred orthotropic lamellar strength limits. (4) The post-yield behaviour is also addressed in a sensitivity analysis by means of an efficient technique, based on the elastic property degradation.

The objective of the work becomes even more important when characterizing the mechanical competence of bone that exhibits certain pathologies. In osteoporosis, for example, the presence of "non-natural" micro pores by the osteoclastic perforation as a consequence of the bone turnover unbalanced process [11–13] is scarcely addressed in literature from a mechanical point of view. These pores, as in any structural material, will undermine the mechanical functionality of bone. In addition, in this pathology, the increase of the mineral content in certain regions causes more heterogeneity and fragile behaviour of bone. In order to deal with these phenomena from a numerical point of view, non-isotropic detailed constitutive models are needed.

The scheme shown in Fig. 1 depicts the work flow of the numerical study carried out in this work. As a starting point, we consider the equations for the estimation of the non-isotropic elastic constants of lamellar tissue as a function of the BMD, developed in a previous authors' work [5]. Subsequently, the influence of the microporosity on the elastic constants is also included explicitly in the numerical models and, therefore, the new homogenization

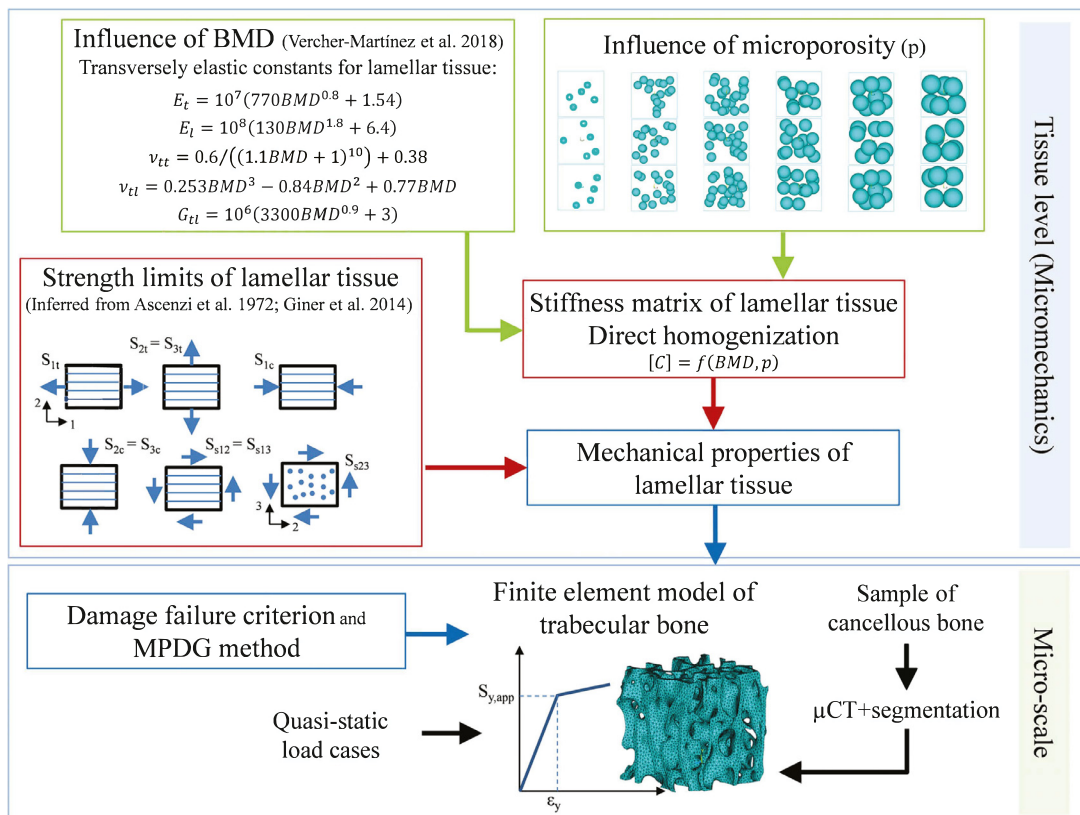


**Fig. 1.** Work flow of the analysis performed in this work, from tissue micromechanics characterization to the  $\mu$ -FE numerical model.

stiffness matrix is derived as a function of BMD and porosity,  $p$ . On the other hand, the tissue strength limits have been inferred from the literature [32,33]. Hence, the resulting mechanical properties of lamellar tissue are applied into the  $\mu$ -FE model of a representative volume of trabecular bone from swine lumbar vertebra. As a first approximation, in the numerical model, the bundles of fibres are oriented following the predominant direction of the trabeculae network. Then, Hashin's orthotropic three-dimensional quadratic failure criterion for fibre composites [34] has been implemented to estimate the onset of the failure in quasi-static displacement-controlled tension and compression numerical simulations. Finally, the damage evolution law follows the MPDG method. A study of the influence of the damage parameters is also performed.

## 2. Methods

### 2.1. Modelling porosity at lamellar tissue

Porosity induces a strong influence on strength and stiffness of bone. These mechanical properties vary inversely with increasing porosity [7,8]. In the following equation, we summarize the three main sources that contribute to the formation of tissue porosity in cortical bone [3]:

$$P_{\text{tissue}} = P_{\text{lac}} + P_{\text{can}} + P_{\text{vas}} \quad (1)$$

where  $P_{\text{lac}}$  is the porosity due to the lacunae, that are small ellipsoids with approximate diameters  $4 \times 9 \times 22 \mu\text{m}$  [35] that contain bone cells (osteocytes).  $P_{\text{can}}$  represents the porosity due to the canaliculi, they are very fine channels radiating from the lacunae. They both constitute the lacunocanicular system that produces a porosity of about 5% [36].  $P_{\text{vas}}$  denotes the vascular porosity that is mainly due to Havers' canals that run the length of osteons together with Volkmann canals and its evaluation depends on the

bone turnover activity. Following the work of Martínez-Reina et al. [3], vascular porosity could vary between 1 and 20%. Consequently, the total porosity for lamellar tissue in cortical bone varies between 6 and 25%. In Eq. (1), the collagen-apatite porosity has been neglected.

Regarding the porosity of lamellar tissue in trabecular bone, lacunocanicular system is also present in the trabecular packets or hemiosteons of cancellous bone. For this term, the same porosity value than in cortical bone is assumed (up to 5%). With respect to the variable  $P_{\text{vas}}$ , marrow cavity harbours the vascularization in trabecular bone, instead of Havers' canals, however, this term is also associated with the bone turnover activity. For trabecular bone, no reference value has been found in literature in order to quantify the microporosity due to the osteoclastic perforation. In this work a value up to 20% will be assumed.

In Fig. 2, the mineralized skeleton of a swine vertebral trabecular bone sample is observed using the Field Emission Scanning Electron Microscope (FESEM) of the Microscope Service at the Polytechnical University of Valencia. These images show that lamellar tissue deposition exhibits a predominant multilayer arrangement. The lamellar nature of the cancellous tissue is clearly manifested at certain regions (Fig. 2a-d). In contrast, some regions show a more homogeneous appearance (Fig. 2e). The lacunocanicular porosity at tissue level is also observed (see Fig. 2f). Furthermore, in Fig. 3 empty lacunae are clearly distinguished.

In the present work, the porosity at tissue level is explicitly modelled by subtracting non-overlapping spheres randomly distributed from a representative elementary volume of lamellar tissue model. The different values of porosity considered are 1, 5, 10, 15, 20 and 25% [3]. In order to obtain averaged properties, 10 models with random distribution of spheres have been analyzed for each value of porosity. In Fig. 4a, three models out of the ten random distributions of voids are shown for each porosity. The numer-

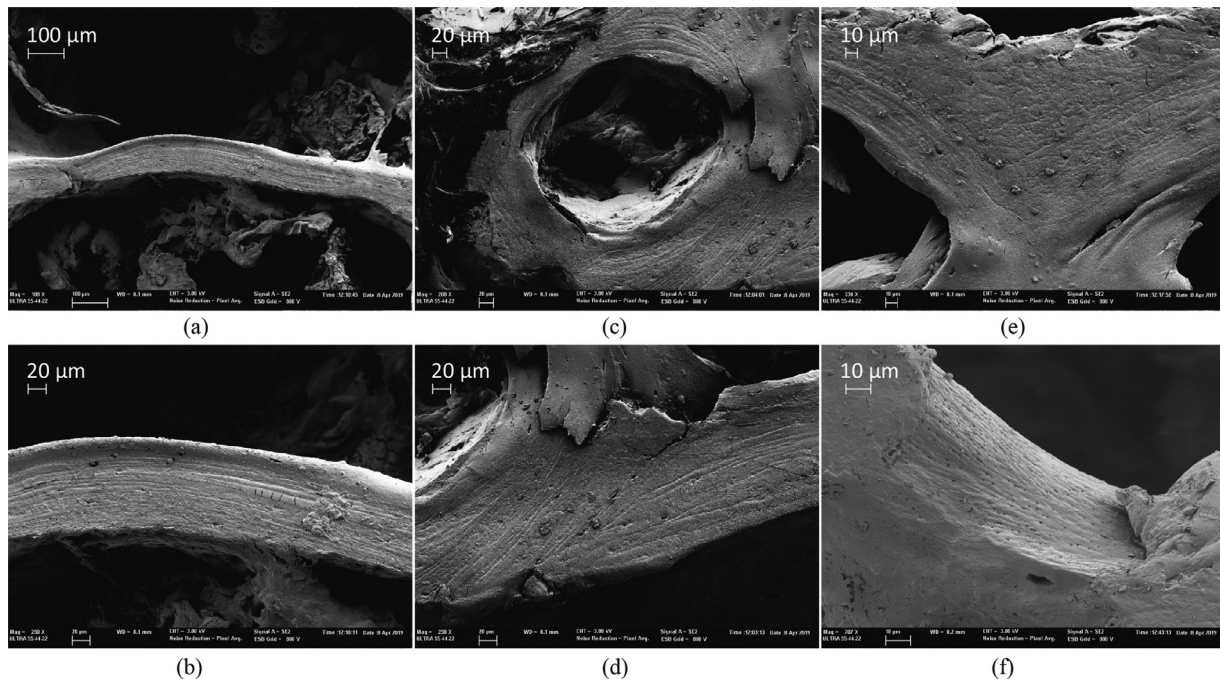


**Fig. 2.** Mineralized skeleton of the lamellar tissue deposition in a swine vertebral trabecular bone sample (Field Emission Scanning Electron Microscope - FESEM) (a) Cross section of a plate structure showing a prone planar multilayer lamellar tissue deposition. (b) A magnification of (a). In (c) lamellar arrangement exhibits a circumferential pattern around a cavity. (d) A magnification of (c). In (e) a branched region is localized showing a more homogeneous tissue arrangement. In (f), the surface of a strut is observed. Microporosity due to lacunocanaliculi system is clearly identified.

ical model of a representative volume of porous lamellar tissue is depicted in Fig. 4b, where the elastic properties for the non-porous part of the lamellar tissue are estimated as a function of BMD, using the equations developed in Vercher-Martínez et al. [5]:

$$E_t^{lam} = 10^7 (770 \text{ BMD}^{0.8} + 1.54) \quad (2)$$

$$E_l^{lam} = 10^8 (130 \text{ BMD}^{1.2} + 6.4) \quad (3)$$

$$\nu_{tt}^{lam} = \frac{0.6}{(1.1 \text{ BMD} + 1)^{10}} + 0.38 \quad (4)$$

$$\nu_{tl}^{lam} = 0.253 \text{ BMD}^3 - 0.84 \text{ BMD}^2 + 0.77 \text{ BMD} + 0.01 \quad (5)$$

$$G_{tl}^{lam} = 10^6 (3300 \text{ BMD}^{0.9} + 3) \quad (6)$$

where  $E$  is the Young's modulus,  $\nu$  represents the Poisson's ratio and  $G$  is the shear modulus. In addition, subscripts  $l$  and  $t$  indicate the longitudinal and transverse directions of the fibre bundles and  $lam$  indicate that the properties are estimated for non-porous lamellar tissue.

In Fig. 4c, the reference system (1,2,3) corresponds to an orientated reference system where 1 indicates the longitudinal direction of the mineralized collagen fibrils ( $l$ ), 2 and 3 are two orthogonal or transverse directions ( $t$ ) of the fibril array. This reference system is only used to set the transversely isotropic elastic properties and strength limits for lamellar tissue.

Cancellous tissue is less mineralized than cortical bone, mainly due to a higher activity of the bone turnover in the trabeculae network. Therefore, considering the work of Koller and Laib [37], the minimum value for the BMD at tissue level is assumed  $0.653 \text{ g/cm}^3$  and the maximum is derived from the work of Yu et al. [38] being  $1.5 \text{ g/cm}^3$ . Table 1 summarizes the numerical values of porosity and BMD at tissue level that have been analyzed in the present work.

In order to estimate the averaged apparent stiffness of the porous lamellar tissue the following procedure has been carried out. First, a direct homogenization technique has been applied by means of the finite element method. Periodic boundary conditions are enforced guaranteeing that the hexahedron analyzed behaves as a continuum domain. The displacement gradients along the corresponding external surfaces must be equal, and, for this purpose, the equations established in Hohe [39] are employed. Assuming the linear elastic Hooke's law (Eq. (7))

$$\sigma_{ij} = C_{ijkl} \epsilon_{kl} \quad (7)$$

where  $\sigma_{ij}$  and  $\epsilon_{kl}$  are the stress and strain tensors, the elements of the constitutive elastic tensor  $C_{ijkl}$  are derived applying six independent unitary strain fields.

Lastly, the elastic constants are explicitly expressed as a function of BMD and porosity,  $p$ , using non-linear multi-variable regressions. These equations will be provided in Section 3.1, and applied to define the elastic properties of lamellar tissue for the  $\mu$ -FE model (see Fig. 4d).

## 2.2. Inferring strength limits of lamellar tissue

In the secondary osteons, lamellae arrange circumferentially around the Havers canal. Within a lamella, mineralized collagen fibrils maintain their orientation constant and change it across the radial direction of the osteon in successive lamellae building the so-called rotated plywood pattern. In the work of Giner et al. [33] the lamellar structure observed in a secondary osteon, was condensed in two equivalent layers: the thin and thick lamellae. In the thin lamella, fibrils are mainly aligned with the circumferential direction of the osteon and in the thick lamella, fibrils are roughly parallel to the long axis of the osteon (see Fig. 5). Thin and thick lamellae do not have any direct application on the trabecular bone numerical model, we use them only to estimate the strength limits of lamellar tissue.

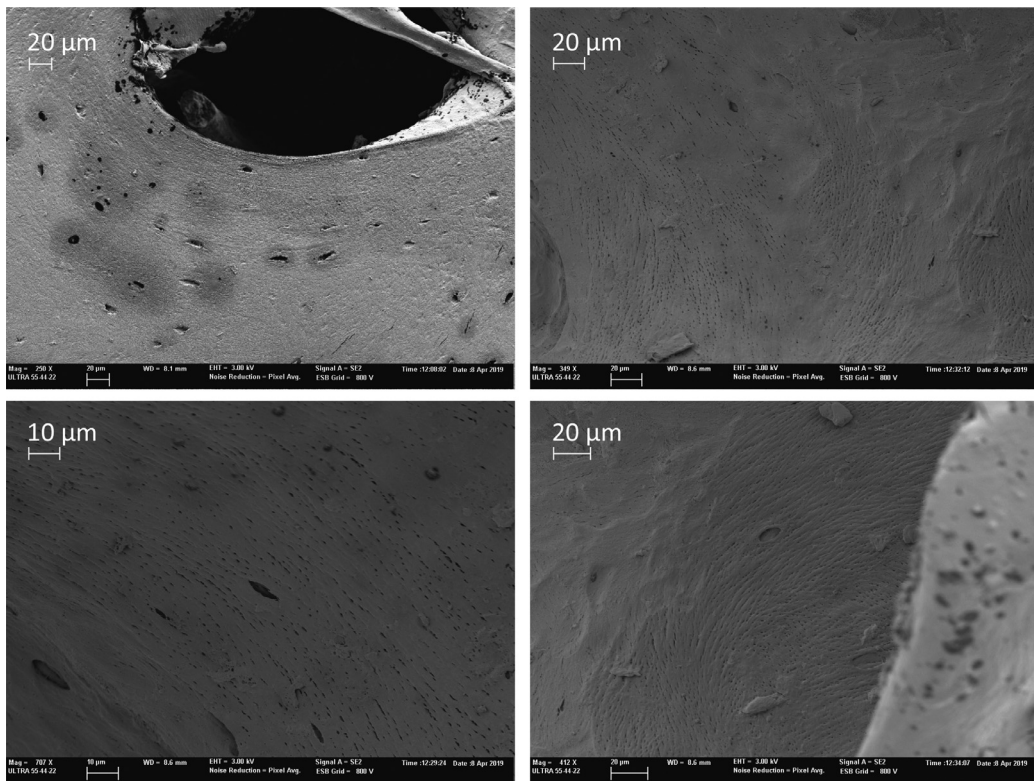


**Fig. 3.** Porosity due to the lacunocanicular system in cancellous bone from swine vertebral sample (Field Emission Scanning Electron Microscope - FESEM).

**Table 1**

Values of BMD ( $\text{g}/\text{cm}^3$ ) and porosity (%) at tissue level considered for estimating the elastic constants of lamellar tissue.

BMD	0.653	0.75	0.85	0.95	1.05	1.16	1.24	1.32	1.39	1.44	1.48	1.50
Porosity	1, 5, 10, 15, 20, 25											

The in-plane strength properties for lamellar tissue were derived relating the results from several works of Ascenzi and Bonucci in which tensile and shear loading were applied on different types of isolated osteons [40,41], with the circumferential  $\sigma_{\theta\theta}$ , radial  $\sigma_{rr}$  and shear  $\sigma_{r\theta}$  stresses (see Fig. 5) and their respective strength limits.

In the current work, the strength limits in an orthotropic material  $S_{1t}$ ,  $S_{2t}$ ,  $S_{3t}$ ,  $S_{23}$ ,  $S_{s13}$  and  $S_{s12}$  depicted in Fig. 6 (following the customary terminology in structural composites materials), are inferred: the circumferential tensile strength  $S_{\theta\theta,t}$  for thin lamellae derived in Giner et al. [33] is corresponding to  $S_{1t}$  and  $S_{\theta\theta,t}$  for thick lamellae corresponds to  $S_{2t}$  and  $S_{3t}$ . Additionally, the shear strength  $S_{r\theta,s}$  for thick lamellae is equivalent to  $S_{23}$  and for thin lamellae represents  $S_{s12}$  and  $S_{s13}$  (see Figs. 5 and 6).

In order to infer the strength limits under compressive loading, the work of Ascenzi and Bonucci [32] has been considered. In their work, the stress-strain curves for compressive loading tests in the longitudinal direction of the osteon were obtained for different degrees of calcification and ages. The experimental analysis were developed for different types of osteons classified, according to the predominant orientation of the mineralized collagen fibrils, in osteons of type I, II and III. In type I osteons, fibrils are mainly orientated in the circumferential direction of the osteon, consequently, the strength limit inferred from the stress-strain curve corresponds to  $S_{2c} = S_{3c}$ . Additionally, in type III osteons, fibrils are mainly aligned with the longitudinal direction of the osteon, hence, the strength limit  $S_{1c}$  can be estimated. The numerical values considered in the current work are averaged from the full calcified samples and are summarized in Table 2.

**Table 2**

Strength limits for full calcified lamellar tissue. Approximated from Ascenzi and Bonucci [32], Giner et al. [33].

$S_{1t} = 120 \text{ MPa}$
$S_{1c} = -115 \text{ MPa}$
$S_{2t} = S_{3t} = 50 \text{ MPa}$
$S_{2c} = S_{3c} = -160 \text{ MPa}$
$S_{s12} = S_{s13} = 46 \text{ MPa}$
$S_{23} = 38 \text{ MPa}$

### 2.3. $\mu$ -FE of trabecular vertebral specimen

The trabecular bone sample was prepared in Instituto de Biomedicina de Valencia (IBV) from lumbar vertebrae of one skeletally mature swine recently euthanised. The parallelepiped-shaped sample, was at least 10 mm side.

The specimen was scanned by  $\mu$ -CT (Skyscan 1172, Bruker, Kontig, Bélgica) at the Estación de Biología Mariña de A Graña (Universidad de Santiago de Compostela, Spain)  $\mu$ -CT service, with an isotropic voxel resolution of  $13.58 \text{ }\mu\text{m}$  (voltage 100 kV, intensity 100  $\mu\text{A}$ , Al/Cu filter).  $\mu$ -CT images were segmented using Scanlp software (Simpleware, UK). Before generating the mesh, the geometrical model was cut leading to a cube-shaped volume with approximately  $2 \times 2 \times 2 \text{ mm}$  side.

$\mu$ -FE mesh was generated using Scanlp Software (Simpleware, UK), leading to a mesh of 3D linear elements. The finite element model of the specimen was able to reproduce with good accuracy the heterogeneous microstructure of cancellous bone (see Fig. 7).

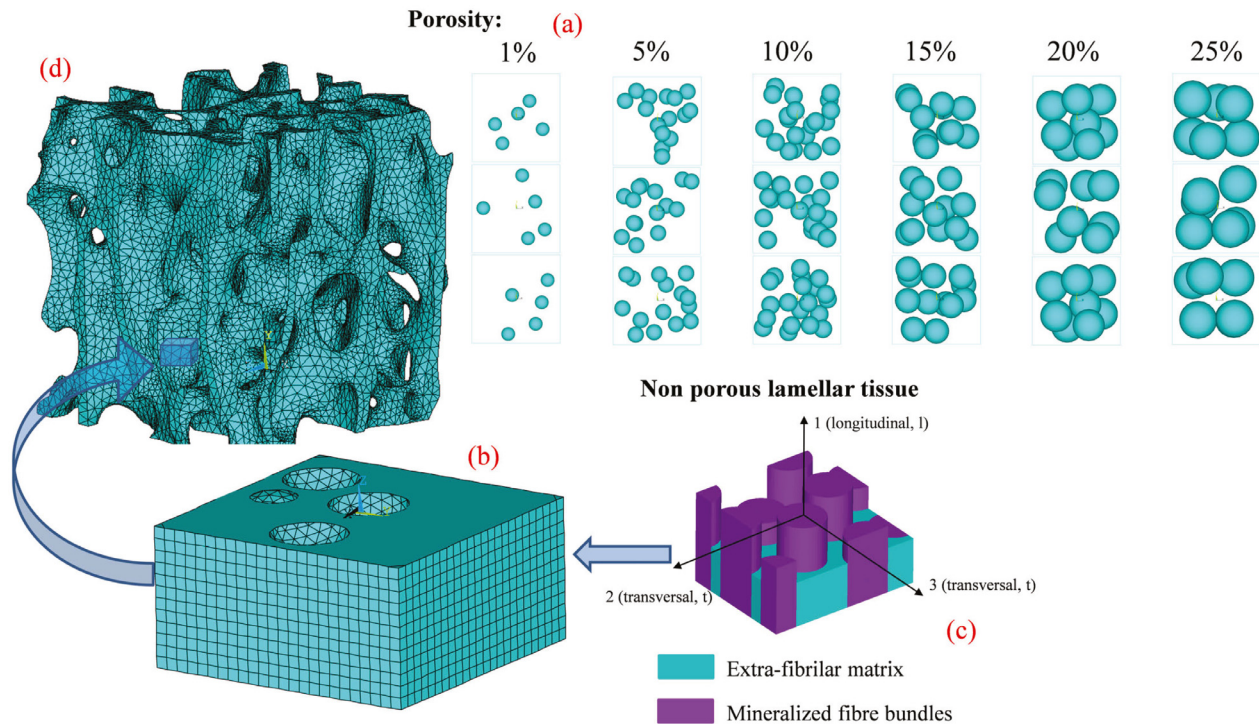


**Fig. 4.** (a) Random distribution of non-overlapping spheres representing the voids. Three examples of the ten models for each level of porosity (plane view projections). (b) Numerical model of the representative elementary volume of porous lamellar tissue. (c) Transversely isotropic elastic properties of lamellar tissue as a function of BMD at tissue level [5]. (d)  $\mu$ -FE model of trabecular bone with homogenized tissue elastic properties. Note that reference system (1,2,3) corresponds to an orientated reference system where 1 indicates the longitudinal direction of the fibrils, 2 and 3 are two transverse directions.

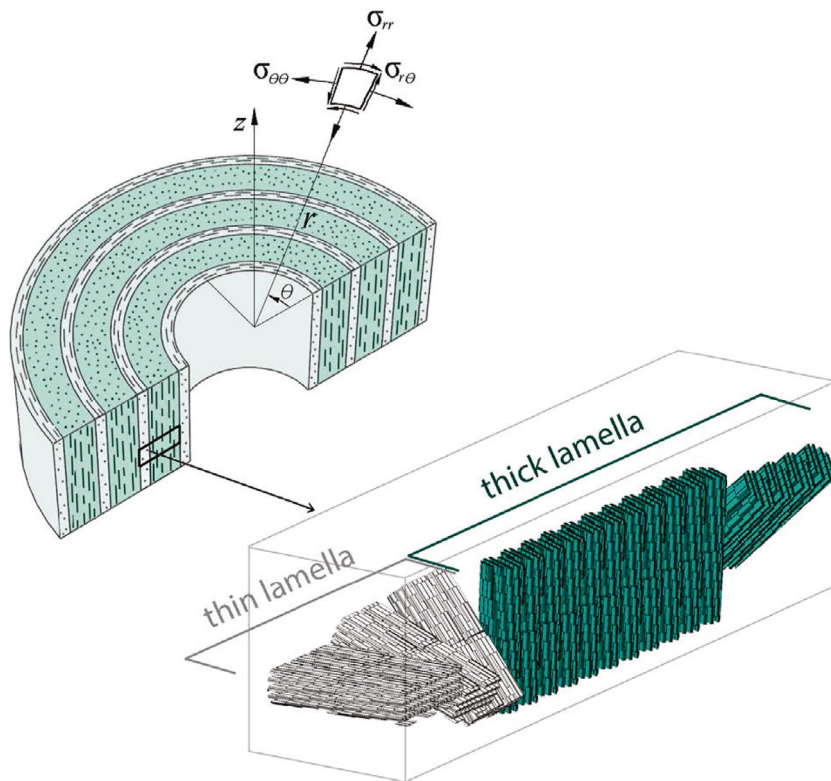


**Fig. 5.** Model of an osteon showing the cylindrical reference system ( $r, \theta, z$ ). The thin and thick lamellae are defined bunching the layers where mineralized collagen fibrils are orientated in a predominant direction [33].

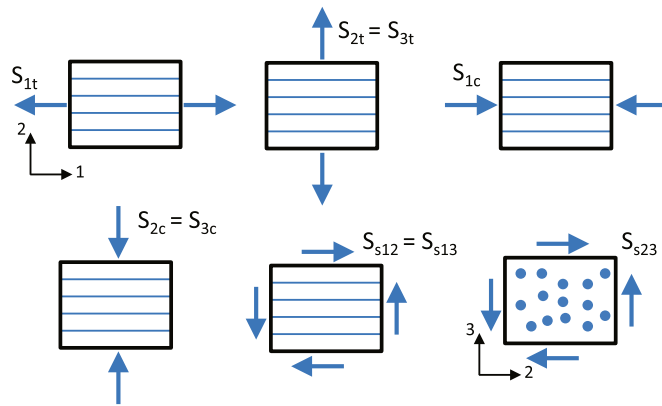


**Fig. 6.** Schematic representation of the strength limits in an orthotropic material following customary terminology in structural composites materials. Reference system (1,2,3) corresponds to the oriented reference system where 1 indicates the longitudinal direction of the fibrils, 2 and 3 are two orthogonal directions (see Fig. 4).

The numerical model is built in a global reference system ( $x, y, z$ ) where loads and constraints will be applied. In this mesoscale finite element model,  $y$  direction denotes the principal bone direction where plates predominate, instead,  $x$  and  $z$  directions show a higher porosity and a foremost strut-like structure.

The stiffness matrix for tissue has been estimated considering the approach developed in this work, assuming uniform reference values for BMD and porosity at tissue level: BMD = 0.85 g/cm<sup>3</sup>, p = 5%. Regarding the strength limits, values summarized in Table 2 are specified in the numerical model. As a first

approximation, we have assumed that the fibril bundles are unidirectionally orientated following the predominant direction of the trabecula [17], consequently, local reference systems are defined with the purpose of considering the non-isotropic lamellar tissue properties, both elastic and strength features, in the  $\mu$ -FE model.

#### 2.4. Bone failure modelling

##### 2.4.1. Orthotropic failure criteria for damage initiation

Considering lamellar tissue as a laminate structure, the Hashin criterion [34], which is widely used in analysis of structural composite materials to predict intralaminar failure, should be an interesting option to analyze the failure initiation at tissue level. The failure Hashin criterion is specially formulated to account for different damage mechanisms. Matrix failure is associated with intralaminar transverse and shear loads, whereas fibre failure is related to longitudinal tension.

The three-dimensional formulation of this orthotropic damage criterion is given by the following equations:

$$f_f = \left( \frac{\sigma_{11}}{X_f} \right)^2 + \frac{(\tau_{12}^2 + \tau_{13}^2)}{S^2}; \quad \sigma_{11} > 0 \quad (8)$$

$$f_f = \frac{\sigma_{11}}{X_c}; \quad \sigma_{11} < 0 \quad (9)$$

$$f_m = \frac{(\sigma_{22} + \sigma_{33})^2}{Y_t^2} + \frac{(\tau_{23}^2 - \sigma_{22}\sigma_{33})}{Q^2} + \frac{(\tau_{12}^2 + \tau_{13}^2)}{S^2}; \quad \sigma_{22} + \sigma_{33} > 0 \quad (10)$$

$$f_m = \frac{(\sigma_{22} + \sigma_{33})}{Y_c} \left[ \left( \frac{Y_c}{2Q} \right)^2 - 1 \right] + \frac{(\sigma_{22} + \sigma_{33})^2}{4Q^2} \\ + \frac{(\tau_{23}^2 - \sigma_{22}\sigma_{33})}{Q^2} + \frac{(\tau_{12}^2 + \tau_{13}^2)}{S^2}; \quad \sigma_{22} + \sigma_{33} < 0 \quad (11)$$

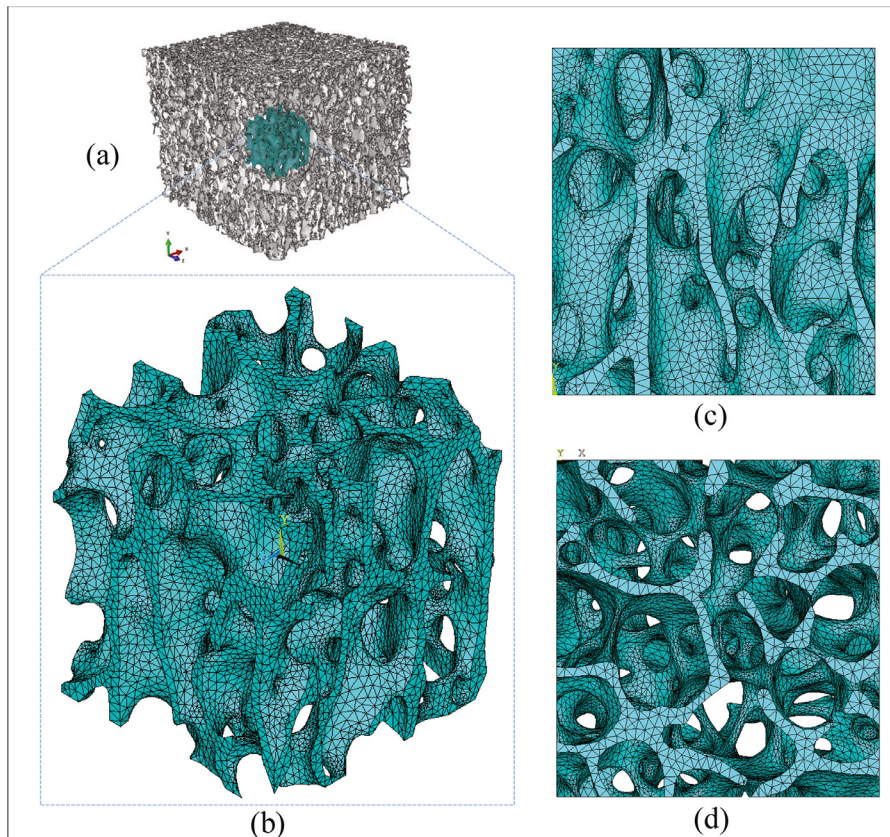


**Fig. 7.**  $\mu$ -FE model of a lumbar vertebra trabecular bone. (a) Geometrical model from segmentation of  $\mu$ -CT images, (b) isometric (c) front and (d) top view. The numerical model has been analyzed with Ansys<sup>®</sup> APDL Software.

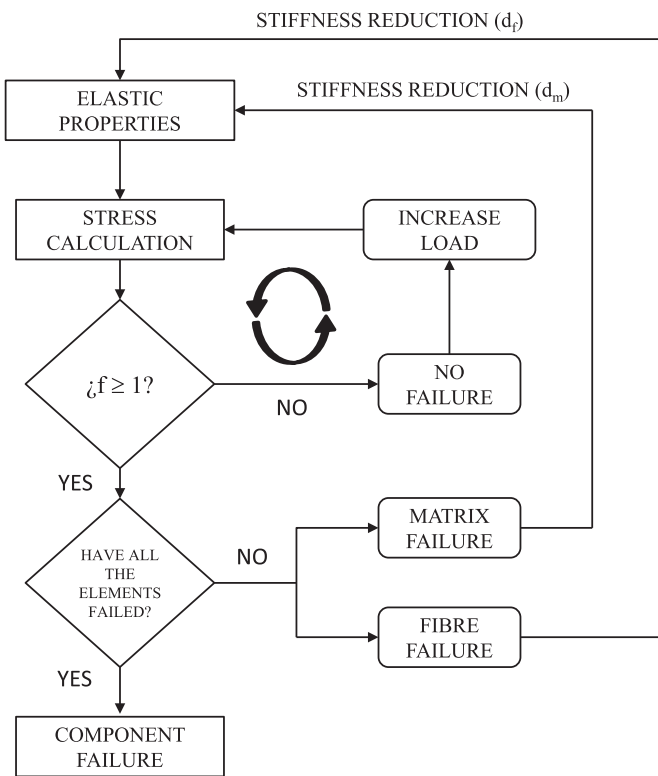


**Fig. 8.** Scheme of the material property degradation MPDG method.

where  $X_t = S_{1t}$ ,  $X_c = S_{1c}$ ,  $Y_t = S_{2t}$ ,  $Y_c = S_{2c}$ ,  $S = S_{12}$  and  $Q = S_{23}$  are the strength limits for lamellar tissue detailed in Section 2.2.

The most critical of the failure modes is selected by means of:

$$f = \max(f_f, f_m) \quad (12)$$

Note that in the above equations,  $f$  denotes the inverse of reserve factor, hence, critical values are greater or equal to one.

## 2.5. Material property degradation MPDG for damage evolution law

Once the failure has initiated, the damage evolution law based on the material property degradation MPDG method is considered. In this smeared crack approach, the discrete domain is as a continuum mesh where the continuity in the displacement field is preserved. In order to reproduce the presence of cracks, the material stiffness is reduced once the failure is achieved accomplishing a certain failure criterion. A scheme of the method implemented is shown in Fig. 8.

This progressive damage model is used to analyze the post-damage degradation of brittle anisotropic materials. The instant stiffness reduction is applied by means of the degradation parameter  $d$  that affects the element stiffness matrix. In the damage model, no tissue properties that could influence on the bone fracture toughness are considered.

Assuming a linear elastic behaviour,  $\tilde{\sigma} = \mathbf{C}\epsilon$  is verified, where  $\tilde{\sigma}$  is the effective Cauchy stress (stress measured in the undamaged domain) and  $\mathbf{C}$  is the undamaged constitutive matrix. Hence, the relationship for a damaged material is given by the following equation:

$$\sigma = \mathbf{C}_d\epsilon \quad (13)$$

where  $\sigma$  is the nominal stress (effective stress averaged over the entire domain, including both damaged and undamaged domains),  $\epsilon$  is the strain and  $\mathbf{C}_d$  is the damaged constitutive matrix. The relationship between the effective stress  $\tilde{\sigma}$  and the nominal can be

found in Barbero and Cabrera [42].  $\mathbf{C}_d$  can be written in terms of the damage variables as follows:

$$\mathbf{C}_d = \begin{pmatrix} \frac{S_{11}}{(1-d_f)} & S_{12} & S_{13} & 0 & 0 & 0 \\ S_{21} & \frac{S_{22}}{(1-d_m)} & S_{23} & 0 & 0 & 0 \\ S_{31} & S_{32} & \frac{S_{33}}{(1-d_s)} & 0 & 0 & 0 \\ 0 & 0 & 0 & \frac{S_{44}}{(1-d_s)} & 0 & 0 \\ 0 & 0 & 0 & 0 & \frac{S_{55}}{(1-d_s)} & 0 \\ 0 & 0 & 0 & 0 & 0 & \frac{S_{66}}{(1-d_s)} \end{pmatrix}^{-1} \quad (14)$$

where  $S_{ij}$  represent the terms of the compliance matrix of the undamaged material  $\mathbf{S}$  and  $d_f$ ,  $d_m$  and  $d_s$  are the fiber, matrix and shear damage variables, respectively. Eq. (14) represents the three-dimensional approach of the stiffness matrix for a damaged unidirectional lamina formulated under the plane-stress assumption in Matzenmiller et al. [43]. Valid values for the damage variables are between 0 and 1, where 0 implies no damage and 1 complete loss of stiffness in the affected mode. This method assumes four damage modes:

$$d_f = \begin{cases} d_f^t & \text{if } \sigma_{11} \geq 0 \\ d_f^c & \text{if } \sigma_{11} < 0 \end{cases} \quad (15)$$

$$d_m = \begin{cases} d_m^t & \text{if } \sigma_{22} + \sigma_{33} \geq 0 \\ d_m^c & \text{if } \sigma_{22} + \sigma_{33} < 0 \end{cases} \quad (16)$$

$$d_s = 1 - (1 - d_f^t)(1 - d_m^t)(1 - d_f^c)(1 - d_m^c) \quad (17)$$

Note that the shear damage variable  $d_s$  is not an independent variable being determined by  $d_f$  and  $d_m$  by means of Eq. (17). Degradation parameters are scalar user-specified quantities. In this work, both the initiation failure criterion and the MPDG method have been implemented in the finite element code using scripts in Ansys APDL. Following a usual procedure in structural composite materials, the nonlinear analyses are performed assuming certain parameter values. A parametric study on the post-yield behaviour has been performed in the current work, considering different values for the damage parameters  $d_f$  and  $d_m$ . For the damage variable associated with the failure due to loads acting on the longitudinal direction of the fibrils, two values have been considered:  $d_f = 0.9$  and  $d_f = 0.9999$ . In laminate strength analysis, fibre failure is usually associated with a severe failure mode, hence, a high value is usually assumed. That means a very important reduction of element stiffness. In fact, the large value of the degradation parameter,  $d_f = 0.9999$ , entails the elimination of the element, producing an overload on the neighbour elements that will not be supported. This situation usually prompts a catastrophic failure. Regarding the damage variable  $d_m$ , this failure mode occurs mainly when loads are acting on the transverse direction of the fibrils or shearing. The numerical values here considered are:  $d_m = 0.5, 0.95$  in the light of the possibility of redistributing the loads when matrix fails, being still able to bear certain level of load, and, finally, the ply discount approach is also considered, being  $d_m = 0.9999$  [42,44]. In this later approach, for the sake of completeness, the stiffness of the element that reaches the damage onset as a consequence of transverse loading, is reduced almost to zero. This technique addresses with the matrix total damage.

## 3. Results

### 3.1. Stiffness of lamellar tissue as a function of BMD and microporosity

In this section, subscript 1 denotes the longitudinal direction of the fibrils, subscripts 2 and 3 represent two orthogonal direc-

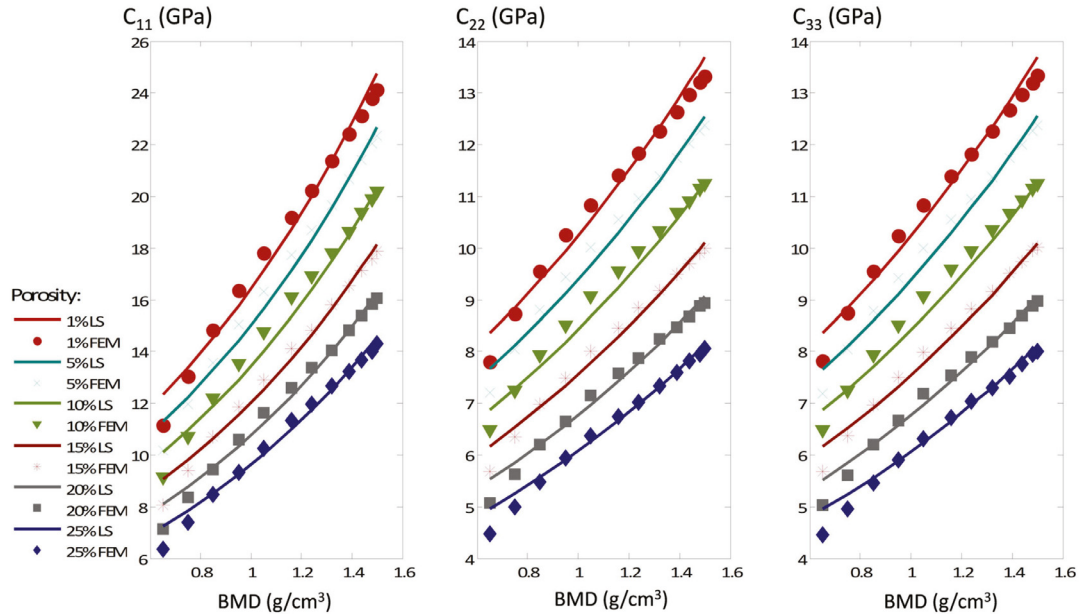


**Fig. 9.** Evolution of the terms  $C_{11}$ ,  $C_{22}$  and  $C_{33}$  of the stiffness matrix for lamellar tissue as a function of BMD and porosity. Markers denote the averaged results from ten numerical homogenized random FE models. Solid lines represent the least square fitting by an exponential function.

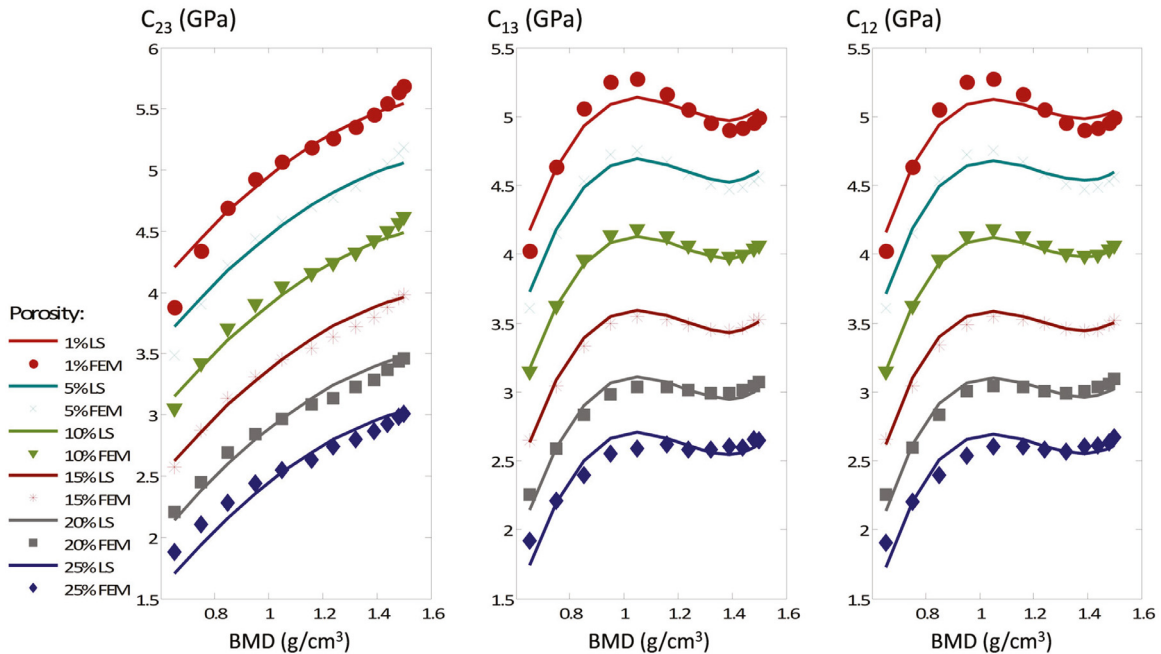


**Fig. 10.** Evolution of the terms  $C_{23}$ ,  $C_{13}$  and  $C_{12}$  of the stiffness matrix for lamellar tissue as a function of BMD and porosity. Markers denote the numerical averaged results from homogenization by FE. Solid lines represent the least square fitting.

tions in the transverse plane of lamellar tissue as shown in Fig. 4. In Figs. 9–11, the orthotropic terms of the symmetric stiffness matrix of lamellar tissue are depicted, as a function of the variables BMD and porosity. The anisotropic terms are negligible. The markers correspond to the averaged results obtained from ten numerical homogenized random models. Nonlinear regressions are shown as solid lines.

As summarized in Table 1, the analysis have been performed for six values of porosity and, for each one, twelve values of BMD. Additionally, as detailed in Section 2.1, for each level of porosity, ten geometrical configurations with randomly distributed voids have been analyzed. For this propose, scripts in *Matlab*® and *Ansys*® APDL have been programmed.

A coherent trend is observed in these results. The higher level of BMD makes the bone stiffer for all porosity values. Likewise, for a given value of BMD, the bone loses stiffness as the porosity increases. It should be highlighted the uniform trend of the principal diagonal terms of the stiffness matrix with both variables, BMD and porosity. A transverse isotropic behaviour is observed, being the stiffest direction coincident with the mineralized collagen fibrils orientation (values of  $C_{11}$  are the highest, whereas  $C_{22}$  and  $C_{33}$  are very similar).

For the sake of clarity, in Fig. 12 the multivariable regressions for the orthotropic terms of the stiffness matrix of lamellar tissue are depicted in three-dimensional plots. Numerical results are represented by blue markers and the regression fitted as a grey surface.

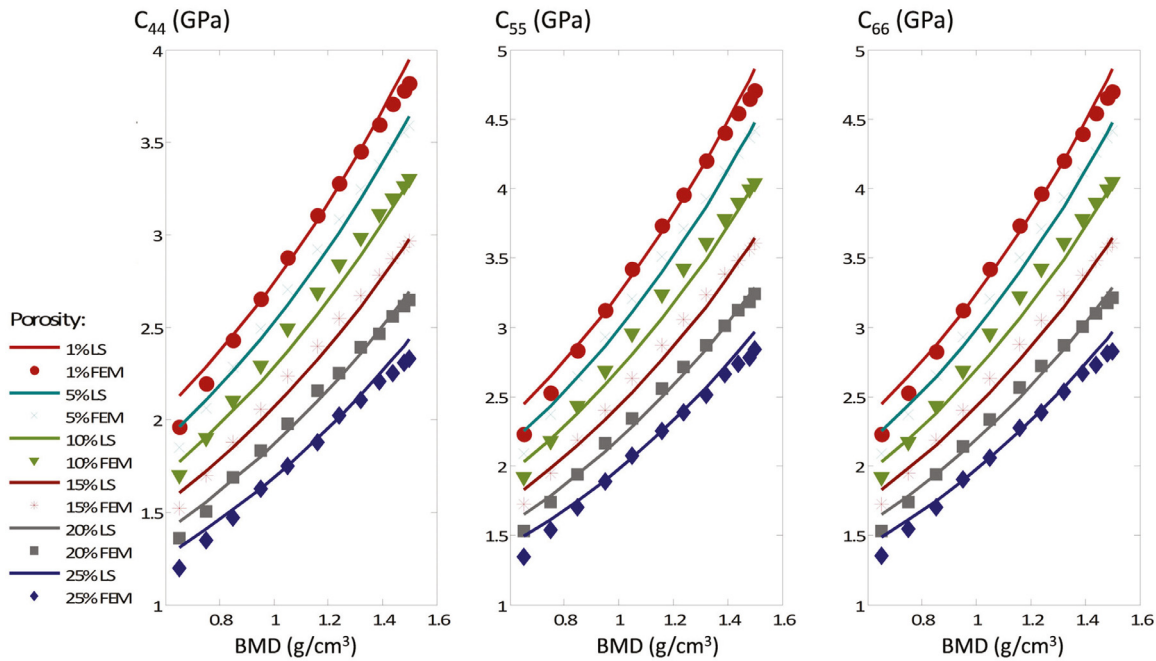


**Fig. 11.** Evolution of the terms  $C_{44}$ ,  $C_{55}$  and  $C_{66}$  of the stiffness matrix for lamellar tissue as a function of BMD and porosity. Markers denote the numerical averaged results from homogenization by FE. Solid lines represent the least square fitting by an exponential function.

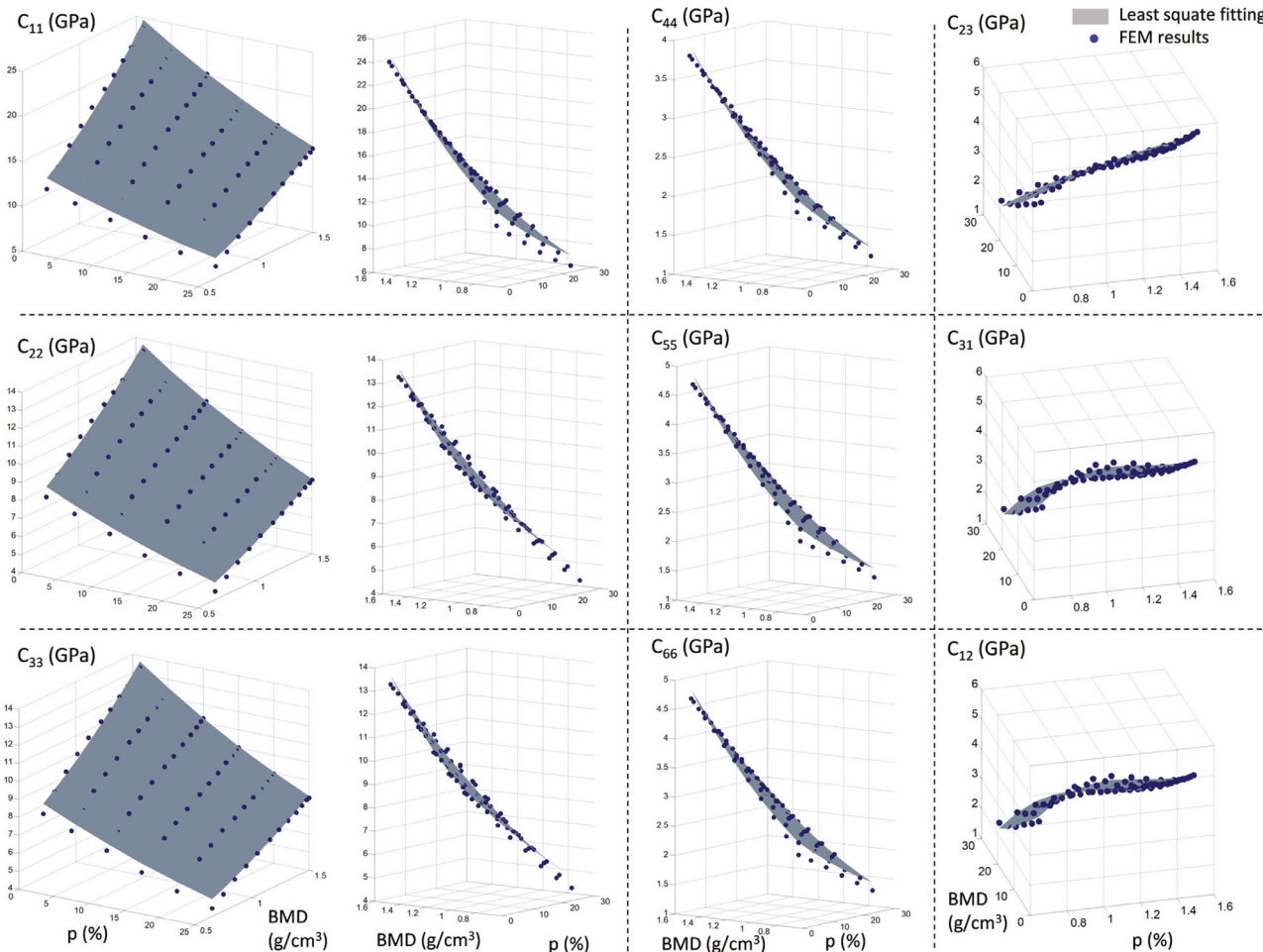


**Fig. 12.** Three-dimensional representation of the orthotropic stiffness matrix terms for lamellar tissue as a function of BMD and porosity.

Subsequently, in order to apply these results in a more general context, the equations that explicitly relate the stiffness terms with the variable BMD and porosity, are derived from the least square fitting (note that results from Eqs. (18) to (23) are expressed in GPa and results from Eqs. (24) to (26) are expressed in Pa):

$$C_{11} = 7.3876 e^{-0.022229 p} e^{0.82134 \text{BMD}} \quad R^2 = 0.99 \quad (18)$$

$$C_{22} = 5.4868 e^{-0.021726 p} e^{0.58165 \text{BMD}} \quad R^2 = 0.99 \quad (19)$$

$$C_{33} = 5.8386 e^{-0.021805 p} e^{0.58304 \text{BMD}} \quad R^2 = 0.99 \quad (20)$$

$$C_{44} = 1.3475 e^{-0.02013 p} e^{0.72977 \text{BMD}} \quad R^2 = 0.99 \quad (21)$$

$$C_{55} = 1.4673 e^{-0.02058 p} e^{0.81231 \text{BMD}} \quad R^2 = 0.991 \quad (22)$$

$$C_{66} = 1.4682 e^{-0.02060 p} e^{0.81189 \text{BMD}} \quad R^2 = 0.991 \quad (23)$$

$$C_{23} = 2.1878 \times 10^9 - 1.2627 \times 10^8 p + 8.4022 \times 10^5 p^2 \\ + 4.0292 \times 10^9 \text{BMD} - 1.1405 \times 10^9 \text{BMD}^2 \quad R^2 = 0.992 \quad (24)$$

$$C_{13} = -6.6623 \times 10^9 - 1.1082 \times 10^8 p - 3.9345 \times 10^5 p^2 \\ + 30227 p^3 + 3.0459 \times 10^{10} \text{BMD} - 2.5596 \times 10^{10} \text{BMD}^2 + 7.0279 \times 10^9 \text{BMD}^3 \quad R^2 = 0.995 \quad (25)$$

$$C_{12} = -3.6721 \times 10^9 - 1.0889 \times 10^8 p - 6.1566 \times 10^5 p^2 \\ + 36350 p^3 + 1.9131 \times 10^{10} \text{BMD} - 1.0812 \times 10^{10} \text{BMD}^2 \\ + 5.8818 \times 10^8 \text{BMD}^3 \quad R^2 = 0.995 \quad (26)$$

### 3.2. Numerical modelling of the trabecular bone strength

In this section, the finite element model of a representative volume of trabecular vertebral bone from a swine specimen (see details in Section 2.3) is analyzed under displacement controlled tension and compression loading. Assuming quasi-static conditions, the bone strength assessment in longitudinal and transversal directions is under scope. Through Eqs. (18)–(26) we estimate the stiffness properties assuming uniform values of BMD and porosity:  $\text{BMD} = 0.85 \text{ g/cm}^3$ ,  $p = 5\%$ . Strength properties for lamellar tissue are summarized in Table 2. As mentioned in Section 2.3, customary reference systems are defined to align the element coordinate systems considering that the mineralized collagen bundles are orientated parallel to the main geometrical feature of the trabecula. Therefore, transversely isotropic elastic properties and strength limits of lamellar bone, defined in an orientated reference system (1,2,3) (see Fig. 4), are currently oriented in the mesoscale model. The bone failure onset and the post-yield regime are analyzed through the Hashin criterion and Material Property Degradation method respectively. Besides, the influence of the damage variables  $d_f$  and  $d_m$  (see details in Section 2.5) is also analyzed. The numerical values considered are  $d_f = 0.9, 0.9999$  and  $d_m = 0.5, 0.95, 0.9999$ .

The graphs shown in Figs. 13–15 outline the stress-strain relationships for the tensile and compressive loading, where the apparent stress is estimated from the resultant force on the supported area in the same direction of the applied displacement. It is remarkable the anisotropic mechanical behaviour of trabecular bone being able to identify approximately an orthotropic trend.

If we compare the results shown in Fig. 13(a) and (b), the damage parameter  $d_f$  presents an important influence on the longitudinal tensile and compressive mechanical behaviour ( $y$  direction of the model). These results are expected because the mineralized bundles of fibres are mainly orientated in that direction. In general, the graphs of Fig. 13(a) show an elastic regime followed by a damage zone where the elements progressively fail simulating the presence of diffuse microcracks. Afterwards, a more generalized element failure is observed suggesting that bone fracture initiates. Further material softening and densification is observed for

$d_m = 0.95$  and 0.9999, whereas strain hardening behaviour is noticeable for  $d_m = 0.5$ . The yield strain can be estimated as  $\epsilon_y^+ = |\epsilon_y^-| = [0.0058 - 0.0071]$ , resulting similar for the different values of  $d_m$  analyzed. The compression yield stress is slightly higher than the tension yield stress, for  $d_m = 0, 5$ :  $S_y^+ = [6.41 - 7.08] \text{ MPa}$  and  $|S_y^-| = [6.41 - 7.22] \text{ MPa}$ .

In Fig. 13(b) a quasi-brittle response is observed for tensile and compressive loading. This situation is promoted by the damage parameter value  $d_f = 0.9999$  that gives rise to the elimination of elements just after failure initiation. The elastic linear zone is followed by a small damage mechanics regime. In this case, we observe that the resistance of the sample in the  $y$  direction is fully conditioned by the strength of the bundles in longitudinal direction, leading abruptly to a catastrophic failure when elements begin to fail. In tensile load, and considering  $d_m = 0.5$ , the yield strain is estimated as  $\epsilon_y^+ = [0.0052 - 0.0068]$ , and for compressive load as  $|\epsilon_y^-| = [0.0056 - 0.0068]$ .

The apparent elastic moduli in the longitudinal direction results equal for both tension and compression loading cases, being estimated in  $E_{y,app} = 1.104 \text{ MPa}$ .

In Figs. 14 and 15 the results for tensile and compressive loading in  $x$  and  $z$  transverse directions are shown. A high influence of  $d_m$  on the post-yielding is observed independently of  $d_f$ . A quasi-brittle behaviour is obtained only when the ply discount is assumed, i.e. removing the element when the transverse failure mode occurs,  $d_m = 0.9999$ . In the other two situations, an important damage mechanism regime is observed. The post-yielding behaviour changes with  $d_m$ . For  $d_m = 0.5$  a strain hardening behaviour is exhibited and for  $d_m = 0.9$  the relationship indicates an increment of elongation at an almost constant stress value without strain hardening regime.

The maximum yield strain is reached for  $d_m = 0.5$ . For this case, it can be defined the elastic limit at the 0.2% of strain. The averaged transverse yield strain is  $\epsilon_y^+ = [0.0079 - 0.0084]$  in tension and  $|\epsilon_y^-| = [0.0075 - 0.0085]$  in compression.

The apparent elastic modulus in the transversal  $x$  and  $z$  directions are estimated as  $E_{x,app} = 292 \text{ MPa}$  and  $E_{z,app} = 252 \text{ MPa}$ . These values are the same both for tension and compression.

In our results, it is observed the quasi-brittle stress-strain behaviour of bone described in Ziopoulos [45] assuming the damage parameter  $d_f = 0.9999$  in case of longitudinal load and  $d_m = 0.9999$  for transverse load. When an element fails, such a large stiffness reduction is equivalent to the elimination of the element, hence the remaining elements are not able to stand the overload, which causes a generalized fail.

On the other hand, regarding the elastic regime, results shown in Table 3 highlight the influence of the non-isotropic elastic properties of lamellar tissue on the elastic behaviour of cancellous bone at mesoscale. Results shown in series with markers are obtained considering Eqs. (18)–(26) for  $\text{BMD} = 0.653, 0.85, 1.05, 1.24, 1.39$  and  $1.48 \text{ g/cm}^3$  and natural values of porosity  $p = 1, 2.5, 5, 7.5$  and 10%.

When isotropic properties for tissue are defined in the numerical model,  $E = 10 \text{ GPa}$  and  $\nu = 0.3$  [46], the apparent moduli result  $E_{x,app}^{iso} = 428.7 \text{ GPa}$ ,  $E_{z,app}^{iso} = 367.9 \text{ GPa}$  and  $E_{y,app}^{iso} = 1164.6 \text{ GPa}$ . As it can be appreciated, stiffness in the transverse directions of the sample ( $x$  and  $z$  directions) can be easily overestimated, particularly for increasing levels of microporosity. In the longitudinal direction ( $y$  direction), the apparent modulus can be reasonably estimated for regular values of BMD and natural microporosity considering isotropic properties for tissue. However, when bone is highly mineralized, the differences increase following a potential law in both variables, bone mineral density and porosity.

Convergence analyses have been performed in order to guarantee the results accuracy. The energy norm of the estimated so-

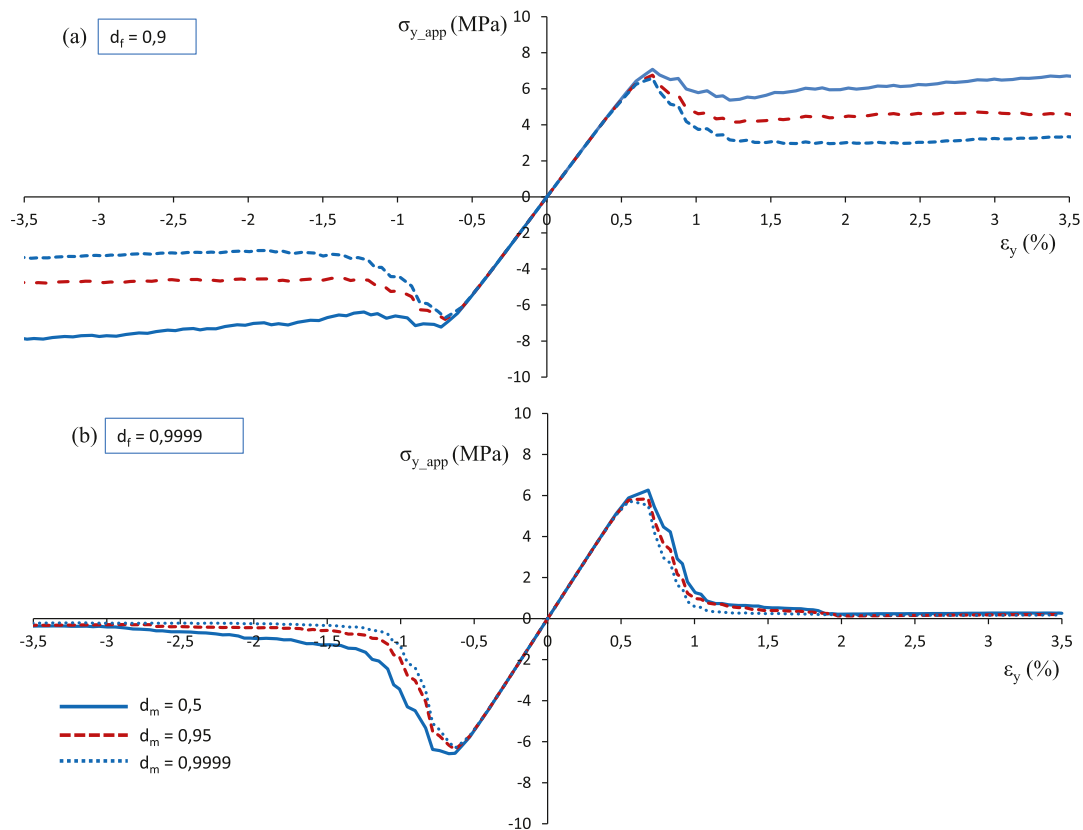


**Fig. 13.** Tensile and compressive stress-strain relationships under displacement control in y direction of the model for (a)  $d_f = 0.9$  and (b)  $d_f = 0.9999$ . Results for different values of the degradation parameter  $d_m = 0.5, 0.95$  and  $0.9999$ .

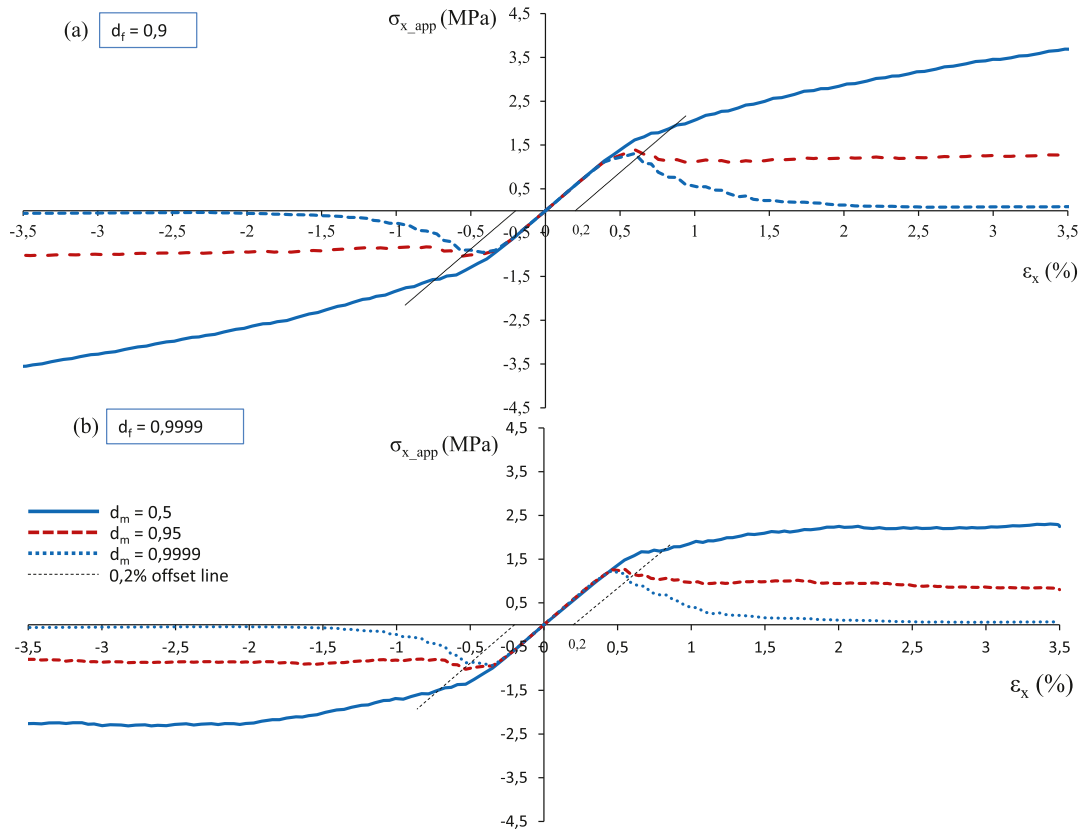


**Fig. 14.** Tensile and compressive stress-strain relationships under displacement control in x direction of the model for (a)  $d_f = 0.9$  and (b)  $d_f = 0.9999$ . Results for different values of the degradation parameter  $d_m = 0.5, 0.95$  and  $0.9999$ .

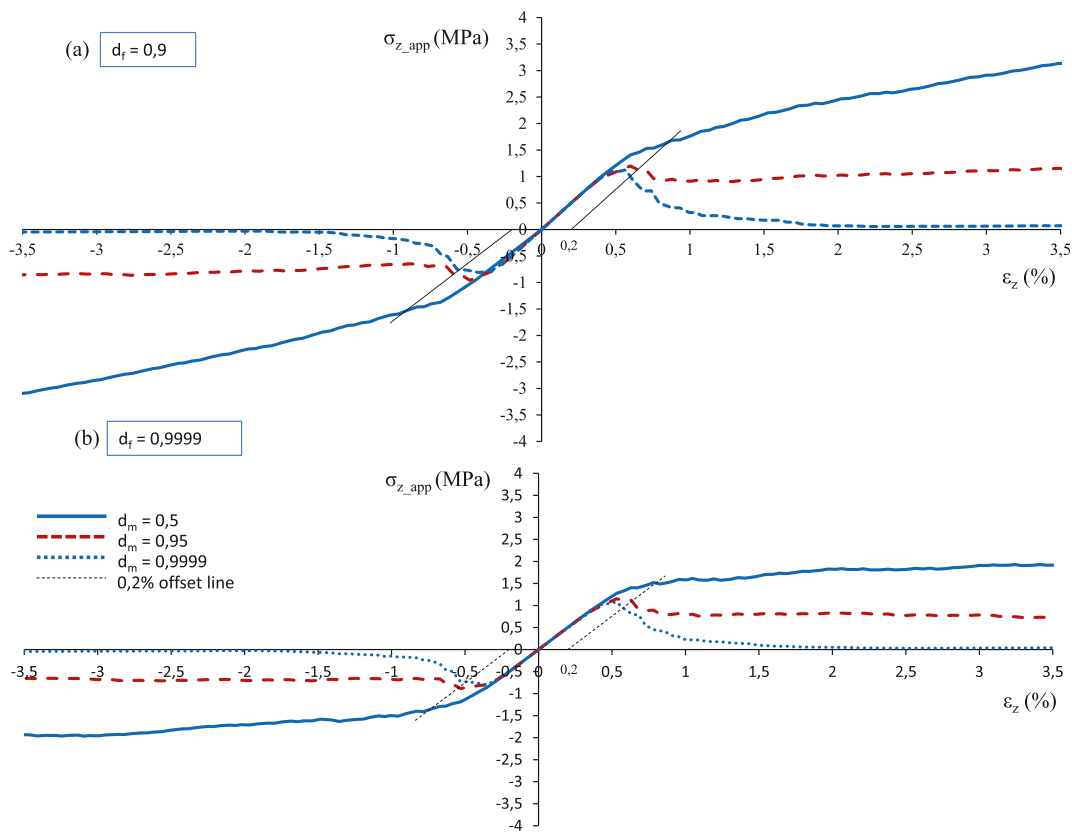


**Fig. 15.** Tensile and compressive stress-strain relationships under displacement control in z direction of the model for (a)  $d_f = 0.9$  and (b)  $d_f = 0.9999$ . Results for different values of the degradation parameter  $d_m = 0.5, 0.95$  and  $0.9999$ .

lution,  $\|U\|$ , has been obtained as a function of the total number of degrees of freedom (DOF) in the numerical model (where  $\|U\| = \sqrt{2\Pi}$ , being  $\Pi$  the computed total strain energy expressed in mJ). The influence of the discretization has been analysed applying a quasi-static compression load in the three orthogonal directions of the sample. To this aim, isotropic properties have been defined in the model. Note that the total DOF may vary slightly for each load case because the number of constraints is different. The strategy is based on a uniform mesh refinement. Values summarized in the Table 4 show that discretization assumed in this work provides accurate results without compromising the computational cost.

In Table 5 the results presented in the current work are summarized, together with reference values found in the literature.

#### 4. Discussion

Bone fracture risk assessment is nowadays a prominent topic of interest in an increasingly aged population. In this sense, many enhancements in high-resolution image acquisition and its treatment have been made to capture the patient specific real architecture of bone. This enables to perform numerical analysis of detailed micro-finite element ( $\mu$ -FE) models. At this point, in most cases, isotropic elastic constants are assumed for tissue modelling, neglecting its anisotropic behaviour, mineral content and the porosity influence on its mechanical response. In fact, isotropic damage continuum approaches are often used to estimate bone failure through numerical modelling [25,26,28,31,46].

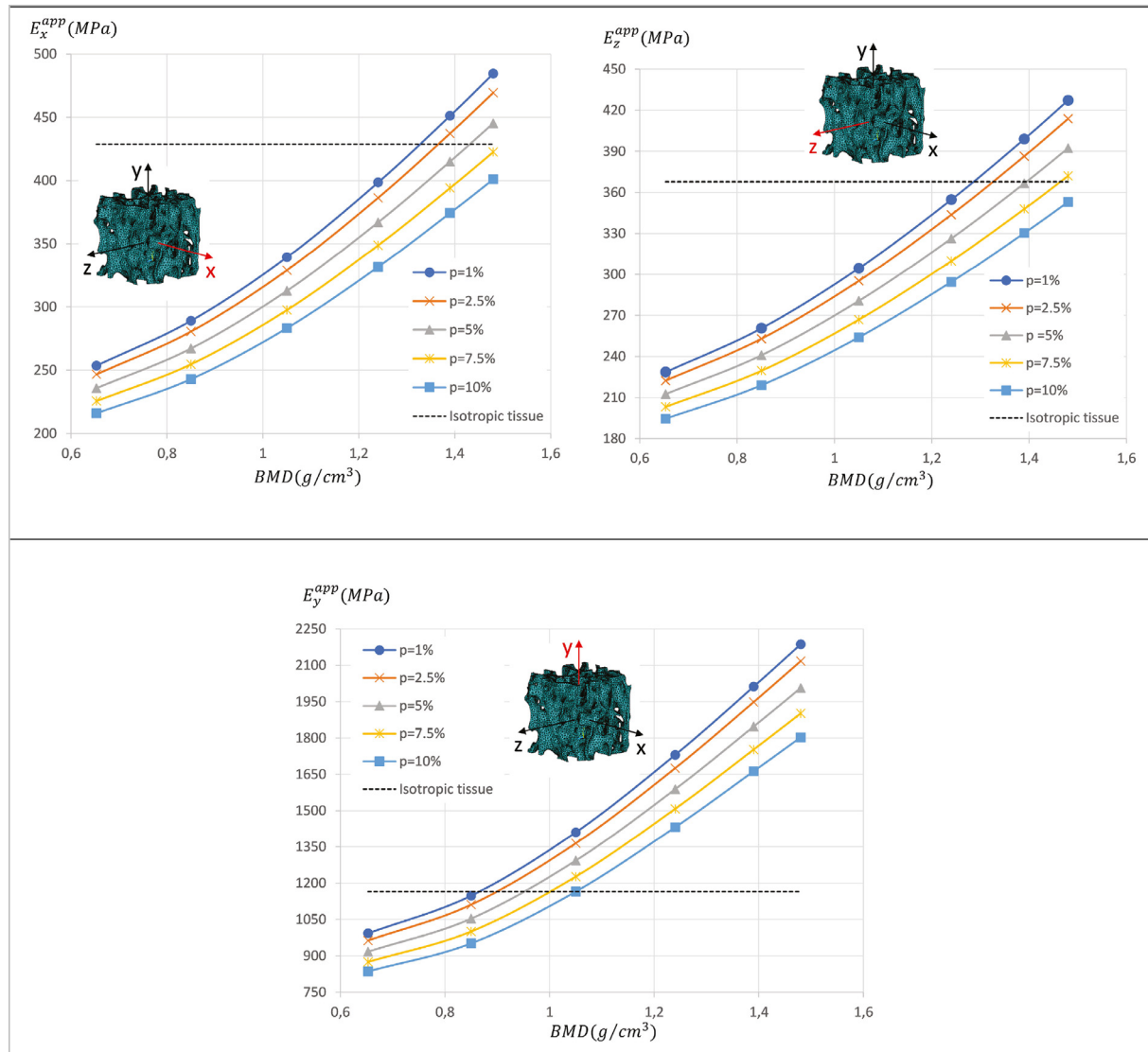
On the other hand, slow bone loss is associated with an incomplete osteoblastic deposition and leads to thinner structural elements. This is one characteristic indicator of an age-related or

senile osteoporotic bone. This bone feature is revealed at micro scale length and can be included in a micro-numerical model obtained from processing  $\mu$ -CT images. Essential morphometric parameters can be then captured. However, a very important impact on the porosity at tissue level is observed when a rapid bone loss accounts as a result of a deeper osteoclastic perforation that can generate discontinuities in the bone structure. This occurs most commonly in postmenopausal women, induced by the abrupt reduction of estrogens [11]. To the authors' knowledge, the influence of the porosity at tissue level on the elastic behaviour of bone has not been addressed in the literature. It is essential to characterize the mechanical properties of bone tissue with prevalence of osteoclastic perforation [13] in the post-menopausal women with osteoporosis, where BMD and microporosity values are altered as a consequence of an unbalanced bone turnover process.

The transversely isotropic model for the elastic tissue properties presented in this work addresses the anisotropic behaviour due to mineralized collagen fibrils orientation, the bone mineral density and microporosity. In addition, in a trabecular bone numerical model at mesoscale, the main fibrils orientation is also considered. In [47], an isotropic Young's modulus for tissue was calibrated from experimental compression tests. Results of that work highlighted that different Young's moduli for tissue in the three orthogonal directions of the sample were to be inferred in order to reproduce the experimental results. A plausible explanation is that the fibrils orientation varies with the direction and this is in consonance with the building substrucures of cancellous bone (plates and rods). Composition, distribution and architecture of lamellar tissue are very important to reproduce the micromechanics failure mode of trabecular bone [20].

**Table 3**

Evolution of the apparent moduli in  $x$ ,  $y$  and  $z$  directions of the cancellous bone numerical model considering two approaches to define the lamellar tissue elastic properties. Results shown in series with markers are obtained considering the Eqs. (18)–(26) presented in this work which estimate the stiffness matrix of lamellar tissue as a function of BMD and porosity at tissue level. The dotted black line shows the numerical solution when isotropic elastic properties are defined for lamellar tissue:  $E = 10$  GPa and  $\nu = 0.3$ , [46].

**Table 4**

Estimated solution in energy norm,  $\|U\|$ , for different discretizations in the  $x$ ,  $y$ ,  $z$  directions. DOF represents the number of degrees of freedom in the numerical model.

x-direction		y-direction		z-direction	
DOF	$\ U\ $	DOF	$\ U\ $	DOF	$\ U\ $
$5.10 \times 10^4$	1.8	$5.10 \times 10^4$	3.0	$5.12 \times 10^4$	1.7
$6.46 \times 10^4$	1.8	$6.39 \times 10^4$	3.0	$6.42 \times 10^4$	1.7
$1.01 \times 10^5$	1.7*	$1.00 \times 10^5$	2.9*	$1.01 \times 10^5$	1.7*
$6.11 \times 10^5$	1.6	$6.11 \times 10^5$	2.9	$6.12 \times 10^5$	1.6
$1.85 \times 10^6$	1.6	$1.85 \times 10^6$	2.9	$1.86 \times 10^6$	1.5

\* Results obtained for the mesh refinement used in this work.

We highlight different novelties of this work: (1) New explicit equations for the estimation of the elastic constants of lamellar tissue are provided. These equations have been obtained as a function of BMD and microporosity in a multiscale analysis, which enable to study the influence of these characterizing parameters on the

mechanical behaviour of bone particularly with certain pathologies, like osteoporosis. (2) The strength limits for fully calcified lamellar tissue have been inferred from literature. (3) The approach herein presented considers the orientation of the mineralized fiber bundles in the trabeculae network, which is essential for the implementation of elastic and strength tissue properties in the numerical model. (4) In accordance to the non-isotropic elastic and strength properties of lamellar tissue, an orthotropic failure criterion is proposed to analyze the damage onset of cancellous bone. The Hashin's interactive failure criterion is considered. (5) The Material Property Degradation (MPDG) method is used to model numerically the damage evolution law at tissue level. A detailed study about the influence of the damage parameters on the mechanical post-yielding response of trabecular bone is also presented.

In Section 3.1, Eqs. (18)–(26) provide the terms of the stiffness matrix of lamellar tissue as a function of two essential tissue parameters, the BMD and the microporosity. In the main terms, a power regression in BMD is observed. There are previous studies that show a similar tendency for the Young's modulus of lamellar

**Table 5**

Results summary. Estimation of yield strain and Young's moduli (apparent values) for trabecular bone and comparison with some reference values from literature.

Longitudinal loading case (y-direction)					
	Tension		Compression		
	This work	Literature	This work	Literature	
Yield strain*	[0.0052–0.0071]	0.0078 ± 0.0004 [48] <sup>(1,m)</sup> [48] <sup>(3,m)</sup> 0.0072 [49] <sup>(1,m)</sup> [46] <sup>(1,c)</sup>	0.0078 ± 0.0004 [48] <sup>(1,m)</sup> 0.0078 ± 0.00041	[0.0052–0.0071]	0.0124 ± 0.00197 [50] <sup>(4,m)</sup> [48] <sup>(3,m)</sup> 0.0084 ± 0.0006 [48] <sup>(1,m)</sup> [0.0046–0.0063] [27] <sup>(3,m)</sup> 0.0081 [49] <sup>(1,m)</sup> 0.00951 ± 0.00125 [46] <sup>(1,c)</sup> 0.00119 – 0.0168 [23,47] <sup>(2,m)</sup>
Young's modulus (MPa)*	1104	384.1 ± 155.1 [49] <sup>(1,m)</sup> 1800 ± 0.058 [19] <sup>(4b,c)</sup>	1017 ± 0.088 [19] <sup>(5a,c)</sup> 908.2 [23] <sup>(2,c)</sup>	1104	309 ± 109 [48] <sup>(1,m)</sup> + 0.088 [19] <sup>(5a,c)</sup> 1800 ± 0.058 [19] <sup>(5b,c)</sup> [47] <sup>(2,m)</sup> 908.2 [23] <sup>(2,c)</sup> 1022.9 [23] <sup>(2,m)</sup>

Transversal loading cases (averaged values for x and z-directions)					
	Tension		Compression		
	This work	Literature	This work	Literature	
Yield strain*	[0.0079–0.0084]	≈ 0.007 [49] <sup>(1,m)</sup> 0.00899 ± 0.00181 [46] <sup>(1,c)</sup>	[0.0075–0.0085]	≈ 0.0082 [49] <sup>(1,m)</sup> 0.0105 ± 0.00115 [46] <sup>(1,c)</sup>	
Young's modulus (MPa)*	252–292	129.7 ± 54.7 [49] <sup>(1,m)</sup> [19] <sup>(5a,c)</sup> 499 ± 63 – 538 ± 70 [19] <sup>(5b,c)</sup> 361.04 – 382.66 [23] <sup>(2,c)</sup>	196 ± 58 – 306 ± 14 [19] <sup>(5a,c)</sup> 499 ± 63 – 538 ± 70 [19] <sup>(5b,c)</sup> 361.04 – 382.66 [23] <sup>(2,c)</sup>	252 – 292 119.5 ± 74.2 [49] <sup>(1,m)</sup> [19] <sup>(5a,c)</sup> 499 ± 63 – 538 ± 70 [19] <sup>(5b,c)</sup> 361.04 – 382.66 [23] <sup>(2,c)</sup>	196 ± 58 – 306 ± 14 [19] <sup>(5a,c)</sup> 499 ± 63 – 538 ± 70 [19] <sup>(5b,c)</sup> 328.1 – 346.0 [23] <sup>(2,m)</sup>

(<sup>1</sup>) Human vertebral trabecular bone. (<sup>2</sup>) Swine vertebral trabecular bone. (<sup>3</sup>) Bovine proximal tibia trabecular bone. (<sup>4</sup>) Bovine distal femora trabecular bone. (<sup>5a</sup>) Human vertebral bone T11/woman/60 years. (<sup>5b</sup>) Human vertebral bone T12/man/56 years. \* Apparent values. m: Mechanical test; c: Computational analysis.

tissue [5,6]. Additionally, we observe an inverse power relationship for the microporosity.

Results summarized in Table 3 show the influence of the non-isotropic elastic properties of lamellar tissue on the apparent moduli of the cancellous bone at mesoscale. When tissue isotropic properties are assumed, stiffness can be frequently overestimated in the transverse directions. In the longitudinal direction, stiffness equally exhibits a high dependence on BMD and microporosity although tissue isotropic properties can be reasonable for values of BMD and microporosity within a natural range.

On the other hand, in Section 3.2, numerical results show that small differences are found for apparent yield strain between tension and compression for the sample analyzed, in agreement with [48,49]. It is known that, although yield strain represents a pretty uniform failure property, it is more influenced by the apparent density in compression than in tension, especially in less dense bone [48]. This can be the main reason for some discrepancies observed in the literature for the apparent yield strain in compression [23,50]. In tension, the apparent yield strain estimated in this work is also in good agreement with values found in the literature (see Table 5), and confirms the tendency to a more uniform value, being less sensitive to the apparent density and anatomical site [47].

In addition, in accordance with [49], no relevant differences between apparent moduli in tension and compression were observed, for both longitudinal and transverse direction of the trabecular bone sample. The apparent elastic moduli estimated in this work are, in general, in good agreement with the values reported in literature [19,23]. However, our results differ from others [48,49]. This can be motivated by differences in the mineral content of the samples, anatomic site, bone volume fraction, shape complexity of the structure or experimental conditions.

Nevertheless, this study presents some limitations. Bone surfaces present a high activity of bone remodelling. Consequently, lamellar tissue is often renewed at surfaces, leading to a lower mineral content than through in the core. Hence, the tissue elastic constants change through a cross section of a trabecula. For example, a higher elastic modulus (between 5 to 12%) was found at the core than at the cortex of a trabecula. Additionally, values for the strength limits of lamellar tissue summarized in Table 2 correspond to fully calcified tissue and assume healthy bone porosity. However, strength limits are strongly dependent on the degree of calcification [32] and on the degree and shape of porosity. Fur-

ther investigations will be necessary to quantify the influence of the presence of micropore on the strength limits for lamellar tissue. These considerations should be addressed in a more general context. As aforementioned, orientation of the mineralized collagen fibrils in the trabeculae network has been estimated based on the main geometrical feature. A more refined strategy would be necessary to automatize the orientation of the elementary coordinate system, considering the predominant geometrical definition [18], but also including information based on the main pattern that osteocyte long axis follows in the microstructure, what effectively will provide information about how mineralized collagen fibrils are aligned. Besides, BMD and porosity vary within the trabeculae architecture and, in contrast, these values have been assumed homogeneous in our numerical mesoscale trabecular bone model. Lastly, the influence of the penalization parameters on modelling the post-yield behaviour has been addressed. However, a more refined mesh should be necessary for a more detailed analysis. Future works are needed to overcome the described limitations.

This work proposes a new methodology to address the mechanical response of trabecular tissue considering orthotropic elastic and strength tissue properties. The quantification of BMD and porosity at tissue level as characterizing tissue parameters needs of future studies to validate this approach.

## 5. Conclusions

The present work addresses the numerical analysis of the mechanical response of cancellous bone including a new approach for the elastic and strength lamellar tissue properties. The non-isotropic elastic behaviour of lamellar tissue deals with the influence of the bone mineral density and, as a novelty, the microporosity or porosity at tissue level. In addition, according to the strength limits inferred from literature, the failure onset is modeled by means of the Hashin failure criterion in combination with the Material Property Degradation (MPDG) method. The value of the degradation parameters can simulate different post yielding scenarios compatible with the bone damage mechanisms observed in literature, as a quasi-brittle failure or significant loss of stiffness, due to smeared crack regions where the presence of multiple microcracks reduces the load transmission capability.

Results show that, when isotropic elastic tissue properties are considered, the anisotropic ratio of the apparent moduli of cancel-

lous bone is, in general, undervalued, particularly when microporosity increases. Not only the microstructure but tissue properties govern the elastic response of bone at the mesoscale.

On the other hand, the yield strain for tension and compression quasistatic loadings has been estimated in the three orthogonal directions of the bone sample. Results indicate that, for the cancellous bone analyzed, there are no significant differences between tension and compression behaviour for each direction. These results are in agreement with several works found in literature (see Table 5) and they are also compatible with the evidence that a higher apparent density in bone results in a higher yield strain in compression than in tension.

To conclude, the approaches presented in the current work enable to deal with a scarcely treated topic from the mechanical point of view: the undermined capabilities of osteoporotic bone due to severe alterations in parameters as BMD and porosity at tissue level. Adaptation of the morphometric parameters at micro scale level is commonly investigated under this pathology, but neglecting the underlying changes at the tissue level.

### Declaration of Competing Interest

The authors declare that they have no known competing financial interests or personal relationships that could have appeared to influence the work reported in this paper.

### Acknowledgements

The authors acknowledge the Ministerio de Ciencia e Innovación and the European Regional Development Fund (FEDER) for the financial support received through the projects PID2020-118920RB-I00 and PID2020-118480RB-C21, the Generalitat Valenciana for Plan FDGENT 2018 and Programme PROMETEO 2021/046.

### References

- [1] A. Nazarian, M. Stauber, D. Zurakowski, B.D. Snyder, R. Müller, The interaction of microstructure and volume fraction in predicting failure in cancellous bone, *Bone* 39 (2006) 1196–1202.
- [2] M.B. Parfitt A. M., B. Chir, Bone remodeling and bone loss: understanding the pathophysiology of osteoporosis, *Clin. Obstet. Gynecol.* 30 (1987) 789–811.
- [3] J. Martínez-Reina, J. Domínguez, J.M. García-Aznar, Effect of porosity and mineral content on the elastic constants of cortical bone: a multiscale approach, *Biomech. Model. Mechanobiol.* 10 (2011) 309–322.
- [4] A.G. Reisinger, D.H. Pahr, P.K. Zysset, Sensitivity analysis and parametric study of elastic properties of unidirectional mineralized bone fibril-array using mean field methods, *Biomech. Model. Mechanobiol.* 9 (2010) 499–510.
- [5] A. Vercher-Martínez, E. Giner, R. Belda, A. Aigou, F.J. Fuenmayor, Explicit expressions for the estimation of the elastic constants of lamellar bone as function of the volumetric mineral content using a multi-scale approach, *Biomech. Model. Mechanobiol.* 17 (2018) 449–464.
- [6] J.D. Currey, Power law models for the mechanical properties of cancellous bone, *Eng. Med.* 15 (3) (1986) 153–154.
- [7] J.D. Currey, The effect of porosity and mineral content on the Young's modulus of elasticity of compact bone, *J. Biomech.* 21 (1988) 131–139.
- [8] M.B. Schaffler, D.B. Burr, Stiffness of compact bone: effects of porosity and density, *J. Biomech.* 21 (1988) 13–16.
- [9] S.M. Tommasini, P. Nasser, B. Hu, K.J. Jepsen, Biological co-adaptation of morphological and composition traits contributes to mechanical functionality and skeletal fragility, *J. Bone Miner. Res.* 23 (2008) 236–246.
- [10] S.C. Manolagas, A.M. Parfitt, For whom the bell tolls: distress signals from long-lived osteocytes and the pathogenesis of metabolic bone diseases, *Bone* 54 (2) (2012) 272–278.
- [11] A.M. Parfitt, Age-related structural changes in trabecular and cortical bone: cellular mechanisms and biomechanical consequences, *Calcif. Tissue Int.* 36 (1984) S123–S128.
- [12] L. Mosekilde, Consequences of the remodeling process for vertebral trabecular bone structure: a scanning electron microscopy study (uncoupling of unloaded structures), *Bone Miner.* 10 (1990) 13–35.
- [13] C. Gentzsch, G. Delling, E. Kaiser, Microstructural classification of resorption lacunae and perforations in human proximal femora, *Calcif. Tissue Int.* 72 (2003) 698–709.
- [14] R. Oftadeh, M. Pérez-Viloria, J.C. Villa-Camacho, A. Vaziri, A. Nazarian, Biomechanics and mechanobiology of trabecular bone: a review, *J. Biol. Eng.* 137 (2015). 010802-1–010802-15
- [15] M. Georgiadis, M. Guizar-Sicairos, O. Gschwend, P. Hangartner, O. Bunk, R. Müller, P. Schneider, Ultrastructure organization of human trabeculae assessed by 3d sSAXS and relation to bone microarchitecture, *PLoS One* 11 (8) (2016) e0159838, doi:10.1371/journal.pone.0159838.
- [16] E. Donnelly, R.M. Williams, S.H. Downs, M.E. Dickinson, S.P. Baker, M.C.H. van der Meulen, Quasistatic and dynamic nanomechanical properties of cancellous bone tissue relate to collagen content and organization, *J. Mater. Res.* 21 (2006) 2017–2106.
- [17] R. Hosaka-Takamiya, M. Hashimoto, Y. Imai, T. Nishida, N. Yamada, H. Mori, T. Tanaka, N. Kawanabe, T. Yamashiro, H. Kamioka, Collagen production of osteoblasts revealed by ultra-high voltage electron microscopy, *J. Bone Miner. Metab.* 34 (2016) 491–499.
- [18] M.A. Hammond, J.M. Wallace, M.R. Allen, T. Siegmund, Incorporating tissue anisotropy and heterogeneity in finite element models of trabecular bone altered predicted local stress distributions, *Biomech. Model. Mechanobiol.* 17 (2018) 605–614.
- [19] H.A. Rami, E. Massarwa, J. Aboudi, F. Galbusera, U. Wolfram, H.J. Wilke, A new multiscale micromechanical model of vertebral trabecular bones, *Biomech. Model. Mechanobiol.* 16 (2017) 933–946.
- [20] M.A. Hammond, J.M. Wallace, M.R. Allen, T. Siegmund, Mechanics of linear microcracking in trabecular bone, *J. Biomech.* 83 (2019) 34–42.
- [21] A.M. Torres, J.B. Matheny, T.M. Keaveny, D. Taylor, C.M. Rimnac, C.J. Hernandez, Material heterogeneity in cancellous bone promotes deformation recovery after mechanical failure, *Proc. Natl. Acad. Sci. USA* 113 (2016) 2892–2897.
- [22] G.A.P. Renders, L. Mulder, G.E.J. Langenbach, L.J. van Ruijven, T.M.G.J. van Eijden, Biomechanical effect of mineral heterogeneity in trabecular bone, *J. Biomech.* 41 (2008) 2793–2798.
- [23] R. Belda, M. Palomar, J.L. Peris-Serra, A. Vercher Martínez, E. Giner, Compression failure characterization of cancellous bone combining experimental testing, digital image correlation and finite element modelling, *Int. J. Mech. Sci.* 165 (2019) 105213, doi:10.1016/j.ijmecsci.2019.105213.
- [24] D. García, P. Zysset, M. Charlebois, A. Curnier, A three-dimensional elastic plastic damage constitutive law for bone tissue, *Biomech. Model. Mechanobiol.* 8 (2009) 149–165.
- [25] R. Hamblin, Micro-CT finite element model and experimental validation of trabecular bone damage and fracture, *Bone* 56 (2013) 363–374.
- [26] R. Hamblin, A quasi-brittle continuum damage finite element model of the human proximal femur based on element deletion, *Med. Biol. Eng. Comput.* 51 (2013) 219–231.
- [27] S. Nagaraja, T.L. Couse, R.E. Gulberg, Trabecular bone microdamage and microstructural stresses under uniaxial compression, *J. Biomech.* 38 (2005) 707–716.
- [28] J.J. Schwedrzik, P.K. Zysset, An anisotropic elastic viscoplastic damage model for bone tissue, *Biomech. Model. Mechanobiol.* 12 (2) (2013) 201–213.
- [29] R. Hamblin, Multiscale prediction of crack density and crack length accumulation in trabecular bone based on neural networks and finite element simulation, *Int. J. Numer. Methods Biomed. Eng.* 27 (2011) 461–475.
- [30] R. Hamblin, Apparent damage accumulation in cancellous bone using neuronal networks, *J. Mech. Behav. Biomed. Mater.* 4 (2011) 868–878.
- [31] J. Lemaitre, A continuous damage mechanics model for ductile fracture, *J. Eng. Mater. Technol.* 107 (1985) 83–89.
- [32] A. Ascenzi, E. Bonucci, The compressive properties of single osteons, *Anat. Rec.* 161 (1968) 377–392.
- [33] E. Giner, C. Arango, A. Vercher, F.J. Fuenmayor, Numerical modelling of the mechanical behaviour of an osteon with microcracks, *J. Mech. Behav. Biomed. Mater.* 37 (2014) 109–124.
- [34] Z. Hashin, Failure criteria for unidirectional fiber composites, *J. Appl. Mech.* 47 (1960) 329–334.
- [35] G. Marotti, Osteocyte orientation in human lamellar bone and its relevance to the morphology of periosteocytic lacunae, *Metab. Bone Dis. Relat. Res.* 1 (1979) 325–333.
- [36] S.C. Cowin, Bone poroelasticity, *J. Biomech.* 32 (1999) 217238.
- [37] B. Koller, A. Laib, Calibration of micro-CT data for quantifying bone mineral and biomaterial density and microarchitecture, *Advanced Bioimaging Technologies in Assessment of the Quality of Bone and Scaffold Materials: Techniques and Applications*, 2007, doi:10.1007/978-3-540-45456-4-5.
- [38] W. Yu, C.C. Glüer, S. Gramp, M. Jergas, T. Fuerst, C.Y. Wu, Y. Lu, B. Fan, H.K. Genant, Spinal bone mineral assessment in postmenopausal women: a comparison between dual X-ray absorptiometry and quantitative computed tomography, *Osteoporos. Int.* 5 (1995) 433–439.
- [39] J. Hohe, A direct homogenization approach for determination of the stiffness matrix for microheterogeneous plates with application to sandwich panels, *Compos. Part B* 34 (2003) 615–626.
- [40] A. Ascenzi, E. Bonucci, The tensile properties of single osteons, *Anat. Rec.* 158 (1967) 375–386.
- [41] A. Ascenzi, E. Bonucci, The shearing properties of single osteons, *Anat. Rec.* 172 (1972) 499510.
- [42] E.J. Barbero, J. Cabrera, Determination of material properties for progressive damage analysis of carbon/epoxy laminates, *Mech. Adv. Mater. Struct.* 0 (2018) 1–10.
- [43] A. Matzenmiller, J. Lubliner, R.L. Taylor, A constitutive model for anisotropic damage in fiber-composites, *Mech. Mater.* 20 (1995) 125–152.
- [44] E.J. Barbero, F.A. Cossio, Determination of material parameters for discrete damage mechanics analysis of carbon-epoxy laminates, *Compos. Part B* 56 (2014) 638–646.

- [45] P. Ziopoulos, Recent developments in the study of failure of solid biomaterials and bone: “fracture” and “pre-fracture” toughness, *Mater. Sci. Eng. C* 6 (1998) 33–40.
- [46] P. Wili, G. Maquer, J. Panyasantisuk, P.K. Zysset, Estimation of the effective yield properties of human trabecular bone using nonlinear micro-finite element analyses, *Biomech. Model. Mechanobiol.* 16 (2017) 1925–1936.
- [47] R. Belda, Mechanical and Morphometric Characterization of Cancellous Bone, Universitat Politècnica de València, 2020 Thesis.
- [48] D.L. Kopperdahl, T.M. Keaveny, Yield strain behaviour of trabecular bone, *J. Biomech.* 31 (1998) 601–608.
- [49] U. Wolfram, H.J. Wilke, P.K. Zysset, Damage accumulation in vertebral trabecular bone depends on loading mode and direction, *J. Biomech.* 44 (6) (2011) 1164–1169.
- [50] C.H. Turner, Yield behavior of bovine cancellous bone, *J. Biomech. Eng.* 111 (1989) 256–260.